Parametric Imaging With PET and SPECT

Jean-Dominique Gallezot , *Member, IEEE*, Yihuan Lu , *Member, IEEE*, Mika Naganawa, *Member, IEEE*, and Richard E. Carson , *Senior Member, IEEE*

Abstract—In molecular imaging modalities such as positron emission tomography (PET) or single photon emission computed tomography (SPECT), parametric imaging is the process of creating fully quantitative 3-D maps of pharmacokinetic parameters from a dynamic series of radiotracer concentration images. An overview of the pharmacokinetic parameters that have been assessed in PET or SPECT studies, and the kinetic models that have been proposed to compute parametric images is presented. Parametric imaging is challenging due to the high level of noise in the raw images obtained from the scanner, and the additional needs to obtain the input function of the kinetic model and to correct for subject motion during the usually long dynamic scans. Methods that have been proposed to assess each of these challenges are been reviewed.

Index Terms—Biomedical imaging, molecular imaging, nuclear medicine, parameter estimation, positron emission tomography (PET), single photon emission computed tomography (SPECT).

I. INTRODUCTION

POSITRON emission tomography (PET) and single photon emission computed tomography (SPECT) are imaging methods that measure the distribution in the body or organ of interest of a radiolabeled tracer previously injected into the subject. These radiotracers are selected to measure physiological parameters such as blood flow [1], glucose metabolism [2], indices of enzyme activity, e.g., dopamine synthesis with ^{18}F-FDOPA [3], concentrations of receptors, transporters or other proteins [4], or tissue properties such as hypoxia [5]. However, the concentration of the radiotracer obtained from the imaging scan is usually not equal, or even directly proportional, to the physiological parameter of interest, since the tracer's tissue concentrations are also dependent on many other factors. Instead the physiological parameter of interest should be extracted by analyzing or modeling the time-activity curve (TAC) of the radiotracer. It is thus (usually) necessary to acquire a time series of images of the tracer concentration (called dynamic images or dynamic data). This modeling is usually performed using compartmental models, or other methods derived from compartmental model theory (see Section II-A for the most common models and methods). This modeling may be done by computing first a TAC for

a region of interest (ROI), and then by applying kinetic analysis to obtain values of the model parameters for the whole ROI. Alternatively, this kinetic analysis can be applied to the TACs of all image voxels, to obtain a map of the parameter(s) of interest in the imaged tissue. This process is called parametric imaging.

Parametric imaging is more challenging than ROI analysis due to the high level of noise in single-voxel TACs, and thus many strategies have been developed to obtain better images, either by optimizing the formulation of the model/analysis (see Section II-B), applying the kinetic modeling directly inside the image reconstruction process (see Section II-C) or applying various noise reduction algorithms (see Section III-B). The other two main challenges for parametric imaging are the measurement of the input function of the kinetic model (see Section III-A) and the need to apply motion correction to avoid artifacts in the parametric images (see Section III-C).

A. Physiological Variables of Interest and Outcome Measures

For each application, the tracer is chosen to focus on one physiological variable of interest, such as the blood flow F, the glucose metabolic rate MR_{glu}, or a receptor concentration B_{max}. The kinetic analysis methods used in SPECT and PET studies typically have one or two main pharmacokinetic parameters that are the achievable outcome measures of the imaging study. These main pharmacokinetic parameters are selected since: 1) they are equal or proportional to the underlying physiological variable of interest and 2) they can be determined with reasonable precision and accuracy. Depending on the application, tissue and tracer properties, and the experimental protocol, several different outcome measures may be determined. For example, PET and SPECT studies can be performed using tracers with either reversible or irreversible kinetics. Irreversible tracers are completely or mostly trapped inside the tissue of interest (at least for the duration of the imaging study), whereas reversible tracers show substantial clearance of tracer within the time frame of the scan. Different outcome measures can be produced for reversible and irreversible tracers. Irreversible tracers are more commonly (but not exclusively) used to measure metabolic or enzymatic processes (e.g., glucose metabolism using ^{18}F-FDG), while receptor studies more commonly employ reversible tracers. Here, we will use the term "receptor" studies when the tracer binds selectively to a protein of interest, which could be a receptor, transporter, enzyme, or any other protein of interest,

and the goal is to assess a value proportional to concentration of the protein. In the following paragraphs, we will introduce the main physiological and pharmacokinetic parameters of interest for imaging studies targeting: 1) blood flow; 2) receptor studies using reversible tracers; and 3) studies using irreversible tracers. Table I contains definitions of all symbols used in this presentation.

The best tracers used to measure blood flow have kinetics that can be well described with the one-tissue compartment (1TC) model [Fig. 1(a)]. In that simple model, exchanges of the tracer between the arterial plasma and tissue are explained by two rate constants K_1 and k_2, and the main outcome measure for blood flow tracers is the tissue uptake rate constant K_1, which is linked to physiological variable of interest, the local blood flow F, by the Renkin–Crone equation [6]

$$K_1 = FE_0 = F\left(1 - e^{-PS/F}\right) \qquad (1)$$

where E_0 is the first pass extraction of the tracer. E_0 is a function of the flow itself, the surface area of the capillaries (S), and the permeability of the capillaries (P). The gold standard tracers to measure blood flow with PET are tracers that diffuse readily in the tissue (high PS factor), such as ^{15}O-H_2O and ^{11}C-Butanol. For these tracers, E_0 is very close to 1, and thus K_1 is very close to the true flow value F, however, these two tracers require a cyclotron on site. Even if extraction is not very high, K_1 can still provide useful flow information; for myocardial blood flow, a routinely used tracer is ^{82}rubidium, which has lower first-pass extraction [7]. The parameter K_1 can also be estimated for radiotracers used to assess other targets than blood flow, and it may provide valuable additional flow information if the first-pass extraction E_0 of these tracers is sufficiently high.

The main physiological parameter of interest for receptor studies is the concentration of the target in the tissue, usually denoted B_{max} (typical unit of nM). A second physiological parameter of interest is the tracer's equilibrium dissociation constant K_d. K_d is equal to the concentration of tracer that would occupy 50% of the targeted receptors, and it expresses the affinity of the tracer for the target (comparing two tracers, a lower K_d value indicates that less tracer is needed to occupy 50% of the receptors, and thus indicates a higher affinity of the tracer for the target).

To introduce the outcome measures used in receptor imaging studies, it is useful to consider the two-tissue compartmental (2TC) model shown in Fig. 1(b). In this model, the rates $k_3(t)$ and k_{off} describe the binding of the radiotracer to the target. k_{off} is the dissociation rate constant of the tracer from the receptor (typical unit of min^{-1}). $k_3(t)$ is equal to the product of the association rate constant k_{on} (typical unit of $min^{-1}nM^{-1}$), the tracer free fraction in tissue f_{ND} (for detailed discussion of this concept, see [8]), and the concentration of the unbound receptors, B_{max}-$C_S(t)$. Here, $C_S(t)$ represents the mass concentration of radioligand, so at tracer doses [i.e., $C_S(t) \ll B_{max}$], this simplifies to just B_{max}. K_d is equal to the ratio k_{off}/k_{on}.

Measuring both B_{max} and K_d is only possible when using nontracer doses of radioligand, i.e., by occupying significant fractions of the binding sites. Indeed, at tracer doses, $k_3(t)$ is

constant and equal to the product $k_{on} \times f_{ND} \times B_{max}$, and thus these three terms, k_{on} (and thus K_d), f_{ND} and B_{max}, cannot be estimated separately. Most imaging studies are performed using only tracer doses of radioligand, and in this case, only indices proportional to B_{max} can be estimated. Also, not all target receptors may be available for binding by the radiotracer. Unavailable receptors may be occupied by another (endogenous) ligand or may be in a tissue compartment not accessible to the radiotracer. Thus, all measurable indices are a function of the concentration of available (unoccupied) receptors $B_{avail} \leq B_{max}$. Then for reversible tracers, the theoretically best equilibrium parameter that can be measured at tracer dose is the binding potential BP_F, which is the ratio of B_{avail} and K_d [8]. However, in practice, even this binding potential BP_F may not be directly measurable, since the radiotracer concentrations measured with PET or SPECT also include nonspecific uptake.

For all reversible tracers, the volume of distribution V_T [8] is an achievable outcome measure [9]. The volume of distribution is the ratio of tracer in the target tissue and in the plasma *at equilibrium*. However, the volume of distribution V_T is not the most desirable outcome measure, since: 1) V_T includes the nonspecific binding in the tissue and 2) estimating it requires measuring the arterial input function, which is an invasive procedure in most cases. If it is possible to measure the nonspecific binding in another region/tissue with identical nonspecific binding and without the receptors of interest (such a region is called a reference region), then it is possible to measure a family of outcome measures called the binding potentials (BPs). Three BPs are commonly used in the literature: 1) BP_{ND}; 2) BP_P; and 3) BP_F [8]. BP_{ND} is linked to the volume of distribution V_T in the target region and to the nondisplaceable volume of distribution V_{ND} (estimated or inferred using the reference region) by the following relationship: $BP_{ND} = V_T/V_{ND} - 1$. V_{ND} represents the ratio of target activity to plasma in the absence of specific binding, i.e., the uptake that is not displaceable by a competing agent. BP_{ND} can be estimated noninvasively with analyses using the reference region as input function. Theoretically, BP_{ND} is the product of BP_F and of the radiotracer free fraction in tissue f_{ND} (for theory and methods to estimate f_{ND} and then BP_F, see [8]). Another index that is frequently used in the literature is the distribution volume ratio $DVR = V_T/V_{ND} = 1 + BP_{ND}$, since this parameter appears naturally in model equations. Finally, though most PET or SPECT imaging studies are performed at tracer dose, it is possible to use nontracer doses of radioligand to compute parametric maps of B_{avail} and K_d [10], [11].

To introduce the outcome measures used for irreversible tracers, it is useful to consider the irreversible 2TC model shown in Fig. 1(c). For irreversible radioligands following this model, the best parameter that can be possibly measured at tracer dose is the trapping rate constant k_3. Measuring this quantity is theoretically always possible using kinetic analysis, but: 1) estimating it requires knowing the explicit structure of the compartment model applicable for the radiotracer and 2) the estimation may be statistically unreliable. The second, and more common, parameter of interest is the net uptake rate constant K_i. While k_3 in the 2TC model expresses the

trapping rate in the irreversible pool from the free pool in tissue, K_i expresses the net trapping rate in the irreversible pool from the free pool in plasma. k_3 is more directly proportional to the receptor concentration or enzymatic rate of interest, while K_i expresses the overall consumption/trapping rate of the tracer by the target tissue. K_i is a parameter that can be estimated with methods that do not require knowing the explicit structure of the model (see Section II-A). Moreover, like V_T for the reversible model, estimates of K_i are often more stable than estimates of k_3. In the case of the 2TC model, the relationship between K_i and k_3 is given by $K_i = K_1 k_3/(k_2 + k_3)$. This term represents the product of the initial tracer uptake (K_1) multiplied by the probability that each tracer molecule becomes trapped ($k_3/(k_2 + k_3)$). For radiotracers such as ^{18}F-FDG used to measure metabolic rates of an endogenous substance (glucose), K_i can be used to compute the tissue metabolic rate.

B. Why Parametric Imaging

As described above, dynamic data from molecular imaging modalities can be used to extract and estimate physiological parameters such as blood flow, metabolism, protein concentrations, etc. This process can be performed on an organ or regional basis, or alternatively on a voxel-by-voxel basis. Specifically, this means extracting a TAC from each voxel, processing it using the appropriate modeling methodology to produce one or more parameter values, and constructing parametric images consisting of these parameter estimates. In this way, the analysis can separate out the different factors that contribute to the radioactivity concentration at any given time into their source components.

An example is shown in Fig. 2 for transverse human brain images from the tracer ^{11}C-AFM [12], which binds to the serotonin reuptake site, i.e., the same site of action of selective serotonin reuptake inhibitors. Fig. 2(a)–(c) shows the radioactivity distribution [standard uptake value (SUV)] at different times postinjection. At early times [Fig. 2(a)], the radioactivity distribution follows blood flow, i.e., higher uptake in the gray matter and lower uptake in the white matter. As time progresses [Fig. 2(b) and (c)], the tracer clears from regions with little or no specific binding of the tracer, so that by the end of the study, the tracer shows focal accumulation in the raphe nucleus, a site in the midbrain which is source of serotonergic fibers. Fig. 2(d) and (e) shows parametric images of the uptake rate constant (K_1) and the volume of distribution (V_T), calculated by applying kinetic modeling methods to each voxel, with the resulting parameter estimates "placed" into their respective places in the images. In this way, there is clear separation of the tracer delivery or flow effects [Fig. 2(d)], from the serotonin transporter measures [Fig. 2(e)]. Note that there is qualitative similarity between Fig. 2(a) and (d), as well as Fig. 2(c) and (e), so that the radioactivity images alone could be clinically or biologically useful. However, the quantification provided by the modeling eliminates many possible confounds of evaluating SUV images, such as subject-to-subject differences in tracer bioavailability. Also, note that the distribution of the serotonin transporters shows very focal uptake in the
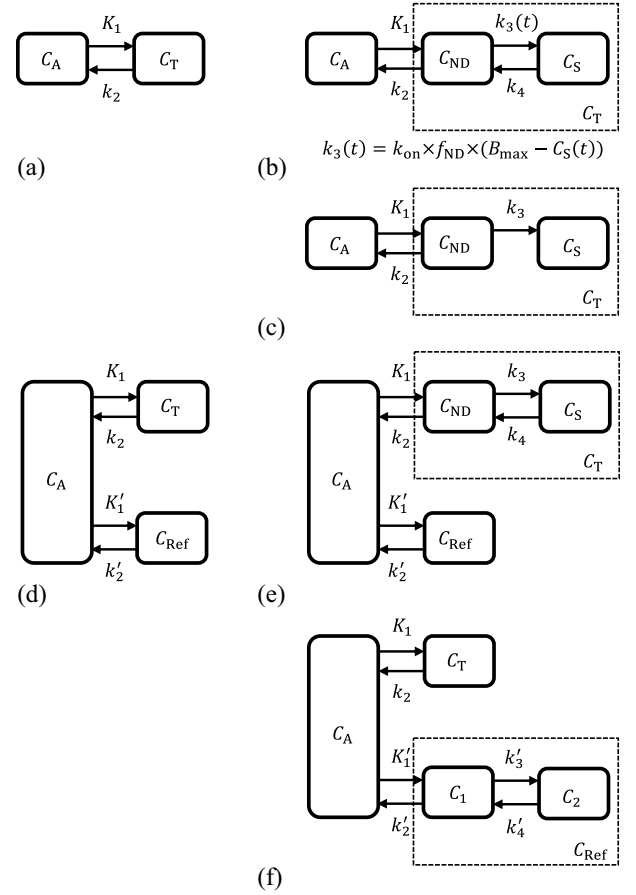

Fig. 1. Main compartmental models used in modeling of PET or SPECT data. (a) 1TC model, describing exchanges between the tissue (concentration C_T) and the arterial input (concentration C_A). This model has two kinetic rate constants K_1 and k_2. (b) 2TC model describing exchanges between the free plus nonspecific pool in the tissue, i.e., the nondisplaceable pool (concentration C_{ND}) and the input C_A, and binding of the radiotracer in a specific compartment (concentration C_S); in this model, the tissue concentration C_T is the sum of the nondisplaceable and specific compartment concentrations. This model has four kinetic rates: K_1, k_2, $k_3(t)$, and k_4. In general, $k_3(t)$ is equal to $k_{on} \times f_{ND} \times (B_{max} - C_S(t))$. $k_3(t)$ becomes a constant at tracer doses, i.e., when $C_S(t) \ll B_{max}$. (c) Irreversible 2TC (2TC-3k) model describing exchanges between the nonspecific pool in the tissue (concentration C_{ND}) and the input C_A, and trapping of the tracer (concentration C_S). This model has only three kinetic rate constants: K_1, k_2, and k_3. (d) SRTM, which assumes that both target and reference tissue can be described by the 1TC model. This model has three parameters: $R_1 = K_1/K_1'$, k_2, and k_2'. (e) FRTM, which assumes that the target can be described by the 2TC model and that the reference tissue can be described by the 1TC model. This model has five parameters: $R_1 = K_1/K_1'$, k_2, k_2', k_3, and k_4. (f) WRTM, which assumes that the target can be described by the 1TC model and that the reference tissue can be described by the 2TC model. This model has five parameters: $R_1 = K_1/K_1'$, k_2, k_2', k_3', and k_4'.

raphe nucleus [hot spot best seen in Fig. 2(e)], so that ROI analysis would likely have missed this heterogeneity.

A second example is shown in Fig. 3 for the glucose metabolism tracer ^{18}F-FDG. The SUV image [Fig. 3(b), activity normalized to dose and body weight] shows a contrast of $\sim$3:1 between the tumor and the normal liver. When modeling is applied to estimate the net uptake rate of ^{18}F-FDG (K_i), the contrast increases to $>$7:1. This difference reflects the different kinetics in the tumor and the liver, as well as the modeling effect of removing the background (unmetabolized
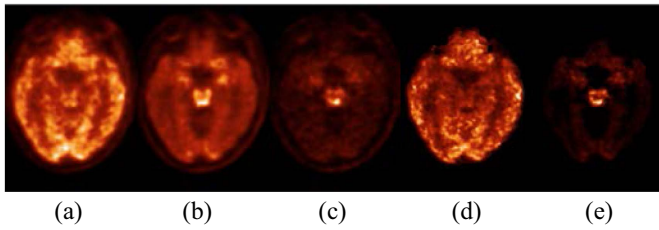
Fig. 2. Images of radioactivity distribution and parametric images from a brain slice using the tracer ^{11}C-AFM. (a) Average image from 0–10 min postinjection. (b) 40–60 min. (c) 90–120 min. (d) Parametric image of uptake rate constant K_1. (e) Parametric image of distribution volume V_T.
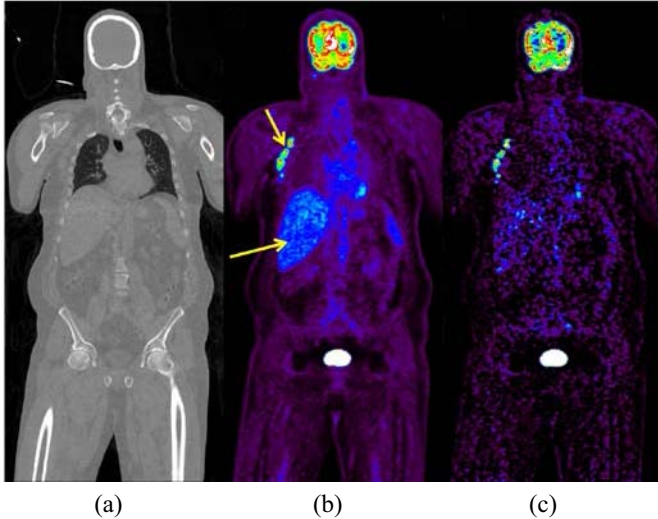

Fig. 3. Images of ^{18}F-FDG in a cancer patient. (a) CT scan. (b) SUV image showing FDG uptake. The lymphoma (upper arrow) has an SUV of 8.9 and the normal liver shows an SUV of 3.2. (c) Parametric image of net uptake constant K_i. Parametric image of uptake rate constant K_i with tumor having value of 28 μL/min/cm^3 and the liver having 3.9 μL/min/cm^3.

^{18}F-FDG) from the image. Again, given the heterogeneity of tumor uptake, proper quantification is best done with parametric images, to assess the maximum tumor uptake, as well as the heterogeneity and other radiomics factors.

There are several other motivations for parametric imaging. Parametric images provide a better mechanism to control and correct for motion in the data, whether it be cardiac, respiratory, or body motion. They are also better suited to account for the partial volume effect and apply partial volume corrections [13]. Also, with novel tracers, images provide the opportunity to both detect metastatic disease, as well as to look for applications of radioactive tracers in other organs. Compared to ROI based analyses, parametric imaging is useful to perform whole-image statistical analyses without relying on a-priori hypotheses about the location of effects or differences [14], or to preform statistical analyses combining the results of the PET or SPECT study with other imaging modalities (e.g., fMRI) to address biological questions which are not solvable with only one modality, especially since combined PET/MR systems are available, which allow to perform simultaneous fMRI and PET studies [15]–[21]. However, there are several challenges that limit the use of parametric imaging. To do the analysis, some form of input function

or reference region must be identified. Further, some amount of dynamic data acquisition must be performed—this can be a serious limitation in a busy clinical environment. Correction for body motion is also critical, as motion can significantly distort a voxel TAC, causing large biases in parametric images. Finally, by extracting more accurate physiological measures from the TAC data, often the noise increases, so careful control of noise is important. Many of these issues are discussed in sections below.

II. MODELS AND METHODS FOR PARAMETRIC IMAGING

A. Basic Models

A variety of analysis methods can be used depending on the tracer's properties (reversible or irreversible tracer; kinetic properties in input and tissue), the availability of a reference region, and the study protocol (e.g., at tracer dose or not; tracer dose is assumed unless stated otherwise). To estimate a rate constant (e.g., K_1) or a composite measure (e.g., K_i), a kinetic analysis needs to be applied. To estimate the volume of distribution V_T or the BP of a reversible tracer, when appropriate, equilibrium-based analyses can be applied for some tracers; otherwise a kinetic analysis is also needed. In this section, kinetic analyses used in PET and SPECT are divided in four main categories: 1) equilibrium methods; 2) compartmental models (Fig. 1); 3) graphical analyses; and 4) spectral analyses. In each case, the methods can be applied to a TAC from a ROI or can be applied voxel-by-voxel to produce parametric images.

1) Equilibrium Analysis and Ratio Methods: The volume of distribution V_T of reversible tracers is the ratio of the tracer concentration in tissue to that in the arterial input at equilibrium. Equilibrium is not readily achieved in an *in vivo* study after a simple bolus injection due to elimination of most tracers from the arterial blood. However, if the radiotracer is infused, a constant concentration may be reached in both target tissue and arterial input: then the volume of distribution V_T can be simply computed by taking the ratio of these two concentrations. Note that "constant" here does not mean constant radioactivity level, i.e., the tracer can be decaying, but a constant decay-corrected activity is maintained. In practice, a bolus plus infusion protocol is used to achieve constant concentrations within the duration of the imaging study. In these bolus plus infusion protocols, the relative size of the bolus compared to the infusion is a critical tuning parameter to ensure that equilibrium is reached with the study time [22]. If applicable, this simple approach can reduce scan time (since it is only necessary to scan after equilibrium is reached) and can produce low-noise parametric images. BP_{ND} can also be estimated using a bolus plus infusion protocol if a reference region is available. However, this simple approach is often not applicable due to unfavorable properties of the tracer: 1) the time needed to reach constant concentrations in both tissue and input may be too long; 2) the optimal bolus plus infusion protocol is too different for some of the tissues of interest; or 3) the optimal bolus plus infusion protocol is too variable from subject to subject. For tracers that clear very slowly, it might not be necessary to infuse the radiotracer since

they can reach a state of transient-equilibrium (also called pseudo-equilibrium) in which: 1) TACs in all tissues and in the input function maintain a constant ratio and 2) the tissue to plasma ratios are equal or relatively close to V_T for all tissues. However, tracers with such favorable properties are very rare. For some tracers, the first condition cannot be achieved since the tracer efflux rate from the tissue is lower (i.e., slower) than the tracer wash-out rate from the body. For some other tracers, the first condition cannot be achieved within an acceptable scan time. Finally, even if condition 1 is achieved, the tissue to plasma ratio at transient equilibrium is higher than V_T unless the tracer efflux rate from the tissue is much larger than the wash-out rate of the tracer from the input [22], [23].

2) Compartmental Models: For reversible tracers which cannot be quantified by equilibrium analysis, or for irreversible or blood flow tracers, a kinetic analysis must be used to compute accurate kinetic parameters or parametric images. The first family of kinetic analyses commonly used is compartmental models. These models have been used for decades for whole-body tracer modeling [24]–[27]. For modeling of nuclear imaging data, the model structure is different, since usually only the target organ and the input or reference are needed (for a dedicated review of compartmental models used in PET, see [9]). For reversible tracers using arterial input function (AIF) data, the main compartmental models are the 1TC and 2TC models [Fig. 1(a) and (b), respectively], which use 2 and 4 kinetic rate constants, respectively. The operational equations for this class of compartment models are the convolutions ($\otimes$) of the AIF $C_A(t)$ with a sum of exponentials (1 per compartment). The equations for the 1TC and 2TC models are, respectively

$$C_T(t) = K_1 C_A(t) \otimes e^{-k_2 t} \qquad (2)$$

$$C_T(t) = \phi_1 C_A(t) \otimes e^{-\theta_1 t} + \phi_2 C_A(t) \otimes e^{-\theta_2 t} \qquad (3)$$

where C_T is the tracer concentration in the target tissue; K_1 and k_2 are the influx and efflux rate constant of the 1TC model; and $\phi_1, \theta_1, \phi_2,$ and θ_2 are coefficients of the impulse response function for the 2TC model [$K_1 \exp(-k_2 t)$ is the impulse response for the 1TC model] and are generally denoted as macro-parameters. $\phi_1, \theta_1, \phi_2,$ and θ_2 are expressed as functions of the kinetic rates $K_1, k_2, k_3,$ and k_4 (the micro-parameters) by the following equations (with $\theta_1 < \theta_2$):

$$\theta_1 = \left(k_2 + k_3 + k_4 + \sqrt{(k_2 + k_3 + k_4)^2 - 4k_2 k_4}\right)/2$$

$$\theta_2 = \left(k_2 + k_3 + k_4 + \sqrt{(k_2 + k_3 + k_4)^2 - 4k_2 k_4}\right)/2$$

$$\phi_1 = K_1(k_3 + k_4 - \theta_1)/(\theta_2 - \theta_1)$$

$$\phi_2 = K_1(\theta_2 - k_3 - k_4)/(\theta_2 - \theta_1). \qquad (4)$$

For reversible tracers, the volume of distribution V_T ($V_T = K_1/k_2$ for 1TC, and $V_T = K_1/k_2(1+k_3/k_4) = \phi_1/\theta_1 + \phi_2/\theta_2$ for 2TC) and the tissue influx rate K_1 can always be estimated [9]. However, estimating all four microparameters of the 2TC model reliably is usually not possible, even using a large ROI TAC (i.e., one with low noise). For most reversible PET and SPECT tracers, the 2TC model is sufficient to fit the tissue

TABLE I
LIST OF PARAMETERS AND PHYSIOLOGICAL VARIABLES

SYMBOL	DEFINITION	UNIT
b	y-intercept of blood-based Logan plot	min
b'	y-intercept of blood-based Logan plot in reference region	min
b'' b'''	y-intercept of reference-based, 2-parameter, Logan plot y-intercept of relative equilibrium plot	min min
B_{avail}	Density of available receptors	nM
B_{max}	Total receptor density	nM
BP_F	Binding potential, defined using free concentration	mL·cm^{-3}
BP_{ND}	Binding potential, defined using non-displaceable concentration	Unitless
BP_P	Binding potential, defined using total plasma concentration	mL·cm^{-3}
C_A	Concentration of radiotracer in arterial blood (metabolite corrected if needed)	nM
C_{ND}	Concentration of free or non-specifically bound radiotracer in tissue	nM
C_{PET}	Measured total concentration of radiotracer in tissue	nM
C_{Ref}	Total Concentration of radiotracer in reference region tissue	nM
C_S	Concentration of specifically bound or trapped radiotracer in tissue	nM
C_T	Total Concentration of radiotracer in tissue	nM
d_i	Duration of the ith PET frame	min
DVR	Distribution volume ratio	Unitless
E_0	First pass extraction fraction	Unitless
F	Blood Flow	mL·min^{-1} ·cm^{-3}
f_{ND}	Tissue free fraction	Unitless
MR_{glu}	Metabolic rate of glucose	mmol ·min^{-1}·cm^{-3}
K_1	Influx rate constant from plasma to tissue or first compartment	mL·min^{-1} ·cm^{-3}
k_2	Efflux rate constant from tissue in 1TC model or from first compartment in 2TC model	min^{-1}
k_2'	Efflux rate constant from reference region tissue	min^{-1}
k_3	Transfer rate from non-specific to specific compartment in reversible or irreversible 2TC model	min^{-1}
k_4	Transfer rate from specific to non-specific compartment in reversible 2TC model	min^{-1}
K_d	Tracer equilibrium dissociation constant	nM
K_i	Tissue uptake rate constant	mL·min^{-1} ·cm^{-3}
k_{loss}	An apparent efflux rate constant from the not perfectly irreversible compartment	min^{-1}
k_{off}	Tracer dissociation rate constant	min^{-1}
k_{on}	Tracer association rate constant	min^{-1}nM^{-1}
P	Capillary permeability	mL·min^{-1} ·cm^{-2}
R_1	Ratio of K_1 values in the target and reference region	Unitless
S	Capillary surface area per unit of volume	cm^2·cm^{-3}
t^*	Start time (from injection time) of a graphical analysis	min
V_E	y-intercept of the Patlak plot	mL·cm^{-3}
V_{ND}	Non-displaceable volume of distribution	mL·cm^{-3}
V_T	Volume of distribution	mL·cm^{-3}
Z^*_i	PET signal from the ith frame in the LEGA model	nM
ϕ_1	Weight of the smallest exponential rate constant of the 2TC model impulse response function	mL·min^{-1} ·cm^{-3}
ϕ_2	Weight of the largest exponential rate constant of the 2TC model impulse response function	mL·min^{-1} ·cm^{-3}
ϕ_i	Weight of the ith exponential rate constant of the spectral analysis model impulse response function	mL·min^{-1} ·cm^{-3}
θ_1	Smallest exponential rate constant of the 2TC model impulse response function	min^{-1}
θ_2	Largest exponential rate constant of the 2TC model impulse response function	min^{-1}
θ_i	i^{th} exponential rate constant of the spectral analysis model impulse response function	min^{-1}

TACs. However, it often leads to unstable V_T estimates, i.e., having high variance. In that case, graphical analysis or spectral analysis methods are often preferred (see below). For some

tracers, the 1TC model is sufficient to fit the tissue TACs and is thus the model of choice.

When a reference region is available, the most frequently used compartmental model is the simplified reference tissue model (SRTM) [28], which assumes that the 1TC model accurately fits the tissue TACs, when using AIF data, in *both* reference and target tissues. The SRTM model has three parameters: $R_1 = K_1/K_1'$, k_2, and k_2' [see Fig. 1(d)]. The operational equation for the SRTM model is

$$C_{\text{T}}(t) = R_1 C_{\text{Ref}}(t) + R_1\left(k_2' - k_2\right)C_{\text{Ref}}(t) \otimes e^{-k_2 t} \quad (5)$$

where C_{Ref} is the tracer concentration in the reference tissue, k_2' is the efflux rate constant of the reference region (' is used to designate parameters for the reference region) and R_1 is the ratio of K_1 values in the target and reference regions. The main physiological parameter of interest of this model, the binding potential BP_{ND}, is computed as $R_1 k_2'/k_2 - 1$. Less commonly used compartmental models are the full reference tissue model (FRTM) [29]–[31] [Fig. 1(e)] and Watabe reference tissue model (WRTM) [32] [Fig. 1(f)], which only assumes that the 1TC model accurately fits tissue TACs in the reference or target tissue, respectively, the other tissue being described by the 2TC model. The FRTM and WRTM are rarely used due to the high number (i.e., 5) of parameters in these two models, which tends to lead to less stable (more variable) BP_{ND} estimates. Thus, when SRTM cannot fit the data, other methods than compartmental models are often used.

For irreversible radiotracers, the only commonly used compartmental model is the irreversible 2TC model (2TC-3k) [Fig. 1(c)], which is the 2TC model, with three rate constants, i.e., the rate constant k_4 is assumed equal to zero.

In all compartment models, extra blood compartments are often required to correct for the activity due to blood in or close to the tissues of interest. Vascular activity contributing to a tissue measurement, either by blood in the tissue, or blood activity spilling in by the partial volume effect are kinetically indistinguishable. For brain imaging, one whole blood compartment is commonly used. For cardiac imaging, two blood compartments are commonly used to correct for the contribution of the right and left ventricles, since the time course in these two blood pools differs, especially at early times postinjection.

3) Graphical Analyses: Graphical analyses were developed to: 1) avoid having to explicitly select the number of compartments in the kinetic models and 2) reduce the number of parameters one needs to estimate, and thus reduce the variability of the main outcome measures. In these methods, the data are transformed so that a plot (Fig. 4) is generated which becomes linear for $t > t^*$, and the main variable of interest is the slope of the line. For reversible tracers, the graphical analyses are called Logan plots (named after Jean Logan). There is one Logan graphical analysis suitable for studies using an AIF [33] [with slope of V_{T}; Fig. 4(b)] and two Logan graphical analyses suitable for studies using a reference region ([34, eqs. (6) and (7)], respectively, with slope of $DVR = 1 + BP_{\text{ND}}$; Fig. 4(c) and (d)). The operational equation

of the blood-based Logan graphical analysis is

$$\frac{\int_0^t C_{\text{T}}(\tau)d\tau}{C_{\text{T}}(t)} = V_{\text{T}}\frac{\int_0^t C_{\text{A}}(\tau)d\tau}{C_{\text{T}}(t)} + b, \quad t > t^* \quad (6)$$

where C_{T} and C_{A} are the tracer concentrations in the target tissue and AIF, respectively, and b is the y-intercept of the Logan plot. This equation only becomes linear at times $t > t^*$, where t^* is determined empirically by assessing when the plot becomes a straight line [Fig. 4(b)]; this time may vary from region to region. Thus, optimal selection of t^* for parametric imaging is complex. This issue is also true for all other graphical analyses introduced below. Typically, one t^* is used for the entire image volume. Please note that if a tracer can be modeled by the 1TC model, then $t^* = 0$ and $b = -1/k_2$.

The operational equation of the first reference Logan graphical analysis can be derived by using (6) for both target and reference regions and eliminating the $\int_0^t C_{\text{A}}(\tau)d\tau$ term. This leads to

$$\frac{\int_0^t C_{\text{T}}(\tau)d\tau}{C_{\text{T}}(t)} = (1 + BP_{\text{ND}})\frac{\int_0^t C_{\text{Ref}}(\tau)d\tau - b'C_{\text{Ref}}(t)}{C_{\text{T}}(t)}$$
$$+ b, \quad t > t^* \quad (7)$$

where b and b' are y-intercepts of the blood-based Logan plots in the target and reference regions, respectively. In the literature, (7) is actually more frequently written by replacing the parameter b' by $-1/k_2'$, by assuming that the reference region TAC can be modeled by the 1TC model and that k_2' is the efflux rate of the 1TC model for the reference region. To use (7) with a simple linear regression approach, the parameter b' (or $-1/k_2'$) must be fixed to an *a priori* value, assuming it is well characterized for the radiotracer in the population under study. If it is variable across subjects and must be estimated in each study, then it is no longer possible to create a plot from (7) and use simple linear regression.

The operational equation of the second Logan graphical analysis is

$$\frac{\int_0^t C_{\text{T}}(\tau)d\tau}{C_{\text{T}}(t)} = (1 + BP_{\text{ND}})\frac{\int_0^t C_{\text{Ref}}(\tau)d\tau}{C_{\text{T}}(t)} + b'', \quad t > t^*. \quad (8)$$

Equation (8) can be derived from (7) by assuming that after some time, the ratio of C_{Ref} and C_{T} becomes constant (transient equilibrium) and thus the term $-b'C_{\text{Ref}}(t)/C_{\text{T}}(t) + b$ becomes a new constant b''. Equation (8) can also be derived directly from compartmental model theory [35]. The Logan graphical analyses require the estimation of only two, in (6) and (8), or three, in (7), parameters, instead of 4 in the 2TC or 5 in the FRTM and WRTM models. However, all graphical analyses require the selection of the time t^* after which the analysis can be applied, which 1) introduces a tuning parameter to optimize, and 2) reduces the number of data points to fit. Moreover, for some tracers with a reference region, the t^* value to use with (8) is quite large in practice, while the t^* value to use with (7) is much lower, and thus (7) is usually the preferred method, even with the additional parameter. For other tracers such as ^{11}C-raclopride, (8) can be used and is the method of choice due to the lower number of parameters.

More importantly in the context of parametric imaging with voxel TACs, these Logan graphical analyses are biased in the presence of a high level of noise in the tissue curves [36], [37]. The bias is caused by violations of the standard assumptions of least squares fitting [38] (see below). Thus, they are not directly applicable for parametric images unless noise reduction is applied to the image data (see Section III-B). Alternatively, methods with less or no noise-induced bias were developed based on these graphical analysis (see Section II-B).

For irreversible tracers, another graphical analysis, known as the Patlak (named after Clifford Patlak) plot [Fig. 4(f)], was developed [39], [40]. Similar to the reversible case, the Patlak plot does not require knowledge of the number of underlying compartments in the model. Two versions of the of the Patlak plot were proposed, one for perfectly irreversible tracers, one for slightly reversible tracers (e.g., with a very small but nonzero k_4 in the 2TC model). The operational equations of these two Patlak plots are

$$\frac{C_T(t)}{C_A(t)} = K_i \frac{\int_0^t C_A(\tau)d\tau}{C_A(t)} + V_E, \quad t > t^* \tag{9}$$

$$\frac{C_T(t)}{C_A(t)} = K_i \frac{\int_0^t C_A(\tau)e^{-k_{loss}(t-\tau)}d\tau}{C_A(t)} + V_E, \quad t > t^* \tag{10}$$

where V_E is the y-intercept of the Patlak plot (E for exchangeable); V_E has the dimensions of a distribution volume; and k_{loss} is a small apparent efflux rate constant from the (not perfectly) irreversible compartment. The first model is more commonly used but the second one may be more accurate for ^{18}F-FDG studies in some tissues and tumors [41], [42]. The two Patlak plots can be used with either an AIF or a reference region devoid of irreversible uptake. Moreover, there is no strong noise-induced bias in the Patlak analysis, since the assumptions of least-squares estimation are not violated (small violations can occur if a noisy reference region curve is used instead of the AIF). However, the Patlak plot cannot be used for all irreversible tracers since it assumes that the reversible pools can reach a state of transient equilibrium (biased or not) within the timeframe of the imaging study [39].

4) Spectral Analysis: Another family of methods that can be used to avoid having to select a precise number of compartments to fit the data is spectral analysis. Compartmental model theory indicates that the impulse response of any compartmental model with AIF can be written as a sum of positively weighted (decreasing) exponentials, that is,

$$C_T(t) = \sum_i \phi_i C_A(t) \otimes e^{-\theta_i t} \tag{11}$$

with $\phi_i > 0$ and $\theta_i \geq 0$. In spectral analysis [43], this property is implemented by using non-negative least square minimization to estimate the positive weights of a family of precomputed basis functions obtained using a predefined range of exponential rates θ. Spectral analysis can also be applied to irreversible tracers by including a basis function with an exponential rate equal to zero. Spectral analysis can also be used for studies using a reference region [35]. However, in this case, compartmental model theory indicates the impulse response function of a compartmental model contains a sum

of exponentials with weights which can be positive or negative. It is thus not possible to use non-negative least square minimization, and other methods are needed to regularize the problem [35].

5) Models for the Nontracer-Dose Case: The methods introduced previously are used for tracer-dose studies. Under tracer conditions, the assumptions of compartment models with constant rates of exchange between compartments are met. However, parametric imaging can also be performed using nontracer dose of radioligand, in order to estimate not only the tracer's volume of distribution or its BP but also the receptor concentration B_{max} and equilibrium dissociation constant K_d. The two commonly used compartmental models have two [44] or three [45] tissue compartments for the radio-labeled tracer. Additional matching compartments are needed for the unlabeled tracer to properly model the time-varying specific activity of the tracer and its effect on $k_3(t)$ [46]. Using these models often requires complex multiple-injection protocols [47], unless simplified analyses can be validated and used [48]. To apply parametric imaging with these models, noise reduction techniques are needed [10], [11]. Parametric imaging using nontracer doses can also be performed using several scans, each performed under equilibrium conditions [49]–[51].

6) Models for the Nonsteady-State Case: Most PET or SPECT studies are performed while the state of the subject is assumed to be invariant during the scan time (e.g., blood flow F or the density of available receptors B_{avail} are assumed to be constant). Conversely, another class of studies is challenge studies where the state of the subject is modified during the scan, either by injecting a drug during the study (e.g., displacement studies) or by stimulating release of the endogenous neurotransmitter (e.g., dopamine for dopamine D2/D3 receptor studies). Models incorporating time-variant pharmacokinetic parameters have been proposed to analyze these studies: most of these models are based on the SRTM model with a time-variant efflux rate constant k_2: LSSRM [52] and lp-ntPET [53], or on the models used for nontracer-dose studies (ntPET [54]) with a time-variant binding rate k_3.

B. Models Optimized for Parametric Imaging

The previous section describes the various compartmental and linearized methods that have been used for analysis of individual TACs, usually from ROIs. Many of these methods are directly applicable and easily implemented on a voxel-by-voxel basis. In general, these models can be divided into three categories.

1) *Group 1:* Model equations that are linear in all parameters.
2) *Group 2:* Model equations with one nonlinear parameter.
3) *Group 3:* Model equations with more than one nonlinear parameter. Such models have not been used widely in parametric imaging to date.

For the linear model equations, as exemplified by Logan *et al.* [33] and Patlak *et al.* [39] analyses described above, the system model can be written as
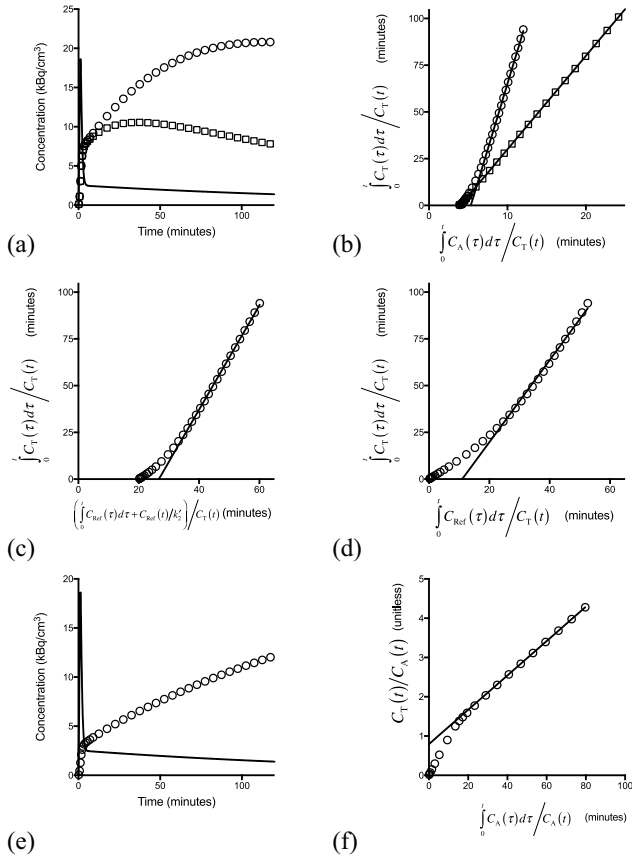
$$\eta = \mathbf{X}\beta \tag{12}$$

Fig. 4.   Sample simulated TACs and corresponding graphical analysis plots. (a) Simulated tissue TACs using the 2TC model (circles) and 1TC model (squares). Solid line shows the blood input curve. (b) Corresponding blood-based Logan graphical analysis for the two simulated TACs shown in (a). In the 1TC case (squares), the plot is linear starting at $t = 0$. Solid lines show the regression lines (with $t^* = 30$ min for 2TC simulation). (c) Corresponding reference-based Logan graphical analysis using (7), computed using the 2TC TAC of (a) for the target tissue and 1TC TAC of (a) for the reference tissue. Solid line shows the regression line (with $t^* = 30$ min). (d) Corresponding reference-based graphical analysis using (8), using the same simulated tissue curves as in (c). Since the ratio of the target and reference TACs used in this simulation does not reach a constant value, the slope of the regression line, i.e., the estimated DVR, is lower using (8) than with (7) for the same t^* setting. (e) Simulated tissue TACs using the 2TC-3k model. Solid line shows the blood input curve. (f) Corresponding Patlak plot using the simulated TAC of (e). Solid line shows the regression line (with $t^* = 30$ min).

where $\boldsymbol{\eta}$ is the n-vector of the model TAC, $\mathbf{X}$ is the n-by-p system matrix, with the columns representing the linearly independent variables, and $\boldsymbol{\beta}$ is the p-vector of unknown parameters to be estimated on a voxel-by-voxel basis. For example, for Patlak analysis, (9) is written in one of the following two forms:

$$\frac{C_\text{T}(t_i)}{C_\text{A}(t_i)} = K_\text{i} \frac{\int_0^{t_i} C_\text{A}(\tau)d\tau}{C_\text{A}(t_i)} + V_\text{E} = K_\text{i}\Theta_i + V_\text{E}, \quad t_i > t^*$$

$$C_\text{T}(t_i) = K_\text{i} \int_0^{t_i} C_\text{A}(\tau)d\tau + V_\text{E}C_\text{A}(t_i)$$
$$= K_\text{i}x_{i,1} + V_\text{E}x_{i,2}, \quad t_i > t^*. \quad (13)$$

In the above formulations, scan frames are indexed by i at times t_i, and the vector of parameters to estimate $\boldsymbol{\beta} = (K_\text{i}, V_\text{E})$, referring to the net influx constant and the exchangeable volume of distribution, respectively. In the first form,

a linear plot can be created, where the time axis is altered from actual time to transformed time Θ. In this Patlak plot, the slope is K_i and the intercept is V_E. The second formulation is the multilinear formula, where the tissue TAC becomes the dependent variable; this version is more natural to add weighting information, based on the variance of the TAC data. For this two-parameter model, each of these cases can be formulated with a system matrix $\mathbf{X}$ composed of two columns. For the multilinear case, column 1 is the integral of the plasma data (from 0 to each mid-frame time) and column 2 is the plasma data interpolated to each mid-frame time. The parameters can be estimated directly using weighted least squares [55]

$$\boldsymbol{\beta} = \left[(\mathbf{X}^t\mathbf{W}\mathbf{X})^{-1}\mathbf{X}^t\mathbf{W} \right]\mathbf{C} = \mathbf{Q}\mathbf{C} \quad (14)$$

where $\mathbf{C}$ is the n-vector of voxel values and $\mathbf{W}$ is a diagonal weighting matrix used to account for different variances of each voxel value (e.g., due to different frame durations, count levels, etc.). The $\mathbf{W}$ matrix is diagonal under the assumption that the statistical noise in each scan frame is independent. A number of different weighting approaches have been developed [56], [57] based on activity in the image, decay, recorded counts, etc. For computational ease, note that the term in square brackets in (14), $\mathbf{Q}$, a p-by-n matrix, is independent of the voxel data $\mathbf{C}$ and can be precomputed, so that the parameter value can be computed extremely efficiently as a dot product of one row of $\mathbf{Q}$ with each voxel vector $\mathbf{C}$.

A simplified linear analytic strategy appropriate for reversible tracers is the Logan plot [33] introduced in Section II-A. Since the model in (6) is linear, production of parametric images of V_T is very computationally efficient. However, under conditions of noisy data, as happens often with voxel data, this method underestimates V_T [36]. The reason for this effect is the violation of two assumptions of least squares fitting: 1) that the independent variable is noise-free and 2) that the dependent variables are statistically independent. Therefore, alternative approaches have been developed, still using linear formulations, but with the tissue concentration $C_\text{T}(t)$ as the dependent variable and integral terms as the independent variables. This reduces the bias, although does not eliminate it completely, since at least one of the independent variables is still noisy. The equation of the multilinear analysis 1 (MA1) method is [58]

$$C_\text{T}(t_i) = -\frac{V_\text{T}}{b} \int_0^{t_i} C_\text{A}(\tau)d\tau + \frac{1}{b} \int_0^{t_i} C_\text{T}(\tau)d\tau$$
$$= \beta_1 x_{i,1} + \beta_2 x_{i,2}, \quad t_i > t^* \quad (15)$$

where b is the same intercept as in the Logan equation and $\beta_1 = -V_\text{T}/b$, $\beta_2 = 1/b$, $x_{i,1} = \int_0^{t_i} C_\text{A}(\tau)d\tau$, and $x_{i,2} = \int_0^{t_i} C_\text{T}(\tau)d\tau$. V_T is then estimated as the negative ratio of the two parameter estimates: $V_\text{T} = -\beta_1/\beta_2$. MA1 allows for efficient computation of parametric images which have less bias.

For reference region methods, the Logan reference method [34] also provides the ability to plot the data as a straight line where the slope is $DVR = 1 + BP_\text{ND}$ (7). However, it also suffers from the same noise-induced bias

as the original, blood-based, and Logan method. The multilinear reference tissue model, MRTM [59] is analogous to MA1 described above and was developed to reduce this bias. The functional equation for MRTM is

$$C_T(t_i) = -\frac{DVR}{b}\left\{\int_0^{t_i} C_{Ref}(\tau)d\tau + C_{Ref}(t_i)/k_2'\right\}$$
$$+ \frac{1}{b}\int_0^{t_i} C_T(\tau)d\tau, \quad t_i > t^*. \tag{16}$$

This equation can be used to fit three parameters (β) to estimate $\beta_1 = -DVR/b$, $\beta_2 = -DVR/(b\,k_2')$, and $\beta_3 = 1/b$, from which BP_{ND} can be determined as $-\beta_1/\beta_3$-1. Alternatively, k_2' can be set to a fixed value and a reduced set of parameters $\beta_1 = -DVR/b$ and $\beta_2 = 1/b$ are determined, with BP_{ND} estimated as $-\beta_1/\beta_2-1$. A subject-specific value of k_2' can be estimated by fitting all the data with the three-parameter MRTM first, and the average or median k_2' value across all voxels can be estimated, and then parameter estimation is performed again with the fixed value of k_2'; this version of the method is denoted MRTM2 [59] and produces less noisy images than MRTM since only two parameters are estimated per voxel in the second step.

For model equations with one nonlinear parameter, rapid voxel-by-voxel calculations are possible, and are generally implemented as a search method. This was first performed in PET [60] for measurement of cerebral blood flow, using the 1TC model, where there was one linear model parameter (K_1) and one nonlinear parameter (k_2) which appears in the exponential term and is convolved with the input function. The general approach for rapid solution of these models is as follows.

1) Define the optimization criterion: $\psi = \sum_{i=1}^{n} w_i(C_T(t_i) - \eta(t_i, \beta))^2$, where the function η is the model equation, $\boldsymbol{\beta}$ is the p-vector of parameters, and w_i are the data weights. Let β_p be the 1 nonlinear parameter.

2) Take the partial derivative of Ψ with respect to the first p-1 elements of $\boldsymbol{\beta}$ and set it to 0. This provides $p-1$ linear equations, allowing the solution for $\beta_1, \ldots, \beta_{p-1}$ in terms of the data vector **C** and the unknown nonlinear parameter β_p.

3) Insert the solutions for $\beta_1, \ldots, \beta_{p-1}$ into the Ψ formula so that it becomes a function of a single variable, β_p.

4) Predefine a set of values for β_p and precompute the relevant tables to make the computation of $\Psi(\beta_p)$ efficient. For example, for the 1TC model, a table of values of the convolution of the input function with $\exp(-k_2 t)$ for each predefined value of k_2 and for each scan time t_i.

5) Search through the table values and find the minimum of the optimization criterion. If desired, interpolate to find the exact minimum value.

6) Use that β_p value to compute $\beta_1, \ldots, \beta_{p-1}$.

In the case of the simplest 1TC model, i.e., one linear (K_1) and one nonlinear (k_2) parameters, the computation of Ψ for each k_2 (β_p) value can be done with a dot product of **C** with a vector from a precomputed table.

One of the most common models used with this approach is SRTM [28] [see (5)] which was implemented with the above approach for creating parametric images, described as a basis function method [61], referred to as RPM. Since SRTM estimates three parameters per voxel, the noise level tends to be higher than that of the 1TC model. To reduce noise, the same approach can be used as mentioned above with MRTM2, i.e., to determine a single value of k_2', which then reduces (5) to a two-parameter model (R_1 and k_2) and thus reduces noise. An example of this application of this strategy is shown for computation of BP_{ND} images for the dopamine D2/D3 receptor radioligand ^{11}C-PHNO (Fig. 5), reducing spurious high BP_{ND} values outside the ROIs known for high D2/D3 concentration, and reducing variability of BP_{ND} values in the ROIs with high D2/D3 concentration. This version is called SRTM2 [62]. Note that the SRTM2 approach depends more strongly on validity of the 1TC assumption in both voxel of interest and reference region, whereas the three-parameter SRTM is more robust to violations of this assumption. In either case, validation of BP_{ND} images estimated with any reference region method compared with those estimated with arterial input data as the gold standard should be performed to assess the suitability of this analysis method for a given radiotracer and application.

Another important model with one nonlinear parameter is the likelihood estimation in graphical analysis (LEGA) method, which, like MA1, is used to reduce the noise-induced bias in the Logan graphical analysis. With MA1, noisy PET data are still used in the independent variables. The integrals in the right-hand side of (15) are less noisy than the original tissue concentration values $C_T(t_i)$, but some noise-induced bias may still be present. To remove (almost all) noisy PET data, a nonlinear method such as LEGA can be used [63], [64]. The operational equation of LEGA is

$$Z_i^* = \frac{\sum_{j=1}^{i-1} Z_j^* d_j + \frac{1}{8} Z_{i-1}^* d_i - V_T \int_0^{t_i} C_A(\tau)d\tau}{b - \frac{3}{8}d_i} \tag{17}$$

where t_i and d_i are the mid-frame time and duration of frame number i, and Z_i^* is the PET signal for frame number i, $\int_{t_i-d_i/2}^{t_i+d_i/2} C_T(\tau)d\tau/d_i$, as computed by the LEGA model for $t_i \geq t^*$, or as measured ($C_T(t_i)$) for $t_i < t^*$. The recursive nature of the LEGA equation stems from the property, $\int_0^{t_i+d_i/2} C_T(\tau)d\tau = \sum_1^i Z_i^* d_i$, which was used to derive the LEGA method. For the analysis of regional TACs, the parameters b and V_T in LEGA can be estimated using an iterative least square fitting algorithm, as performed for compartmental models. In the context of parametric imaging, LEGA can be considered to have one nonlinear parameter b and one linear parameter V_T and the basis-function strategy used for the 1TC and SRTM models can be applied to LEGA [63].

There are a few other models or strategies used to reduce bias or increase computation speed that should be considered. First, another method has been proposed to reduce the noise-induced bias in the Logan graphical analysis. Assuming that the tissue is at transient equilibrium (constant ratios between tissue regions and between tissue and blood), the noisy tissue curve in the denominator of (6) may be replaced by the
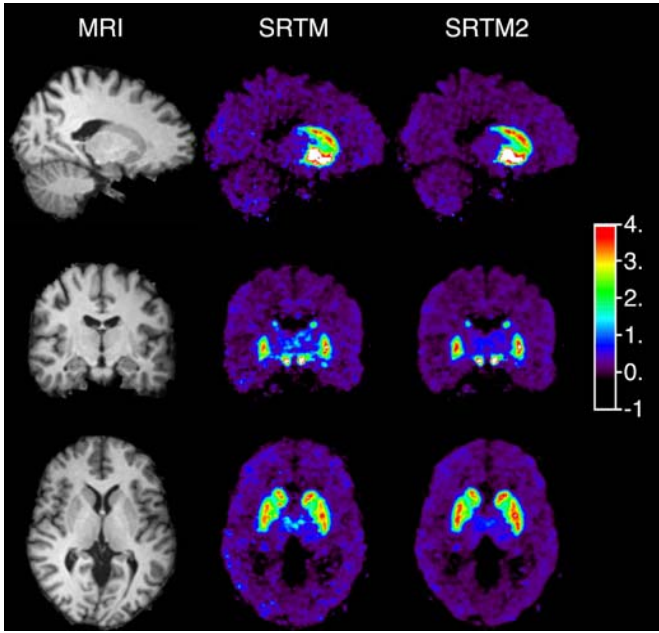
Fig. 5.   Example of noise reduction strategy for ^{11}C-PHNO BP_{ND} images computed using the SRTM model. SRTM2 aims to reduce the noise in SRTM parametric images by reducing the number of fitted parameters from three parameters per voxels to two parameters per voxels plus one global parameter (k'_2).

plasma input curve, leading to the following equation:

$$\frac{\int_0^t C_T(\tau)d\tau}{C_A(t)} = V_T \frac{\int_0^t C_A(\tau)d\tau}{C_A(t)} + b''', \quad t > t^* \qquad (18)$$

where b''' is the y-intercept of the new plot. Due to the extra assumption about transient equilibrium, this method is not a simple rearrangement of the original Logan graphical analysis, but a new graphical method, called the relative equilibrium plot [65]. For most tracers, transient equilibrium is achieved at time greater than t^* in the original Logan graphical analysis. Thus, appropriate t^* values in the relative equilibrium tend to be larger than in the original Logan plot. The relative equilibrium plot can also be seen as a method to correct for the potential bias of the tissue-to-plasma ratio for tracers [22] at transient equilibrium.

In the context of parametric imaging, another general approach has been used to reduce computation time: linearizing the nonlinear equations of compartmental models. Linearization can also be used to take advantage of available analytical solutions when regularization is used to reduce image noise (see Section III-B). From this point of view, MRTM, with $t^* = 0$, is a linearization of the SRTM equation. Similarly, MA1, with $t^* = 0$, is a linearization of the 1TC model equation. This strategy was first used to compute 1TC parametric maps, especially in blood flow studies [66] using the following equation:

$$C_T(t) = K_1 \int_0^t C_A(\tau)d\tau - k_2 \int_0^t C_T(\tau)d\tau \qquad (19)$$

which is identical to the MA1 equation (15) with the following changes of variables: $k_2 = -1/b$ and $K_1 = -V_T/b$. Linear equations have been similarly proposed for the 2TC

model in the MA2 method [58]. For parametric imaging with the models used in some neurotransmitter release studies, LSSRM and lp-ntPET, both linearization and basis-function approaches were used to reduce computation time [52], [53]. However, this linearization strategy has the drawback of potentially introducing bias in the parametric maps due to the noisy independent variables. To reduce this bias, the generalized linear least square (GLLS) method has been proposed for the linearized 1TC model [67] and for the linearized 2TC model [56]. However, the GLLS method is an iterative procedure, which introduces two drawbacks: 1) the optimal number of iterations must be determined, or a stopping criterion must be selected and 2) the computation time is much larger than when using linear least squares, and almost similar to that of the basis-function approach for the 1TC model [68].

Finally, it was observed that in the linear approaches presented previously, the main outcome parameter of interest is not always one of the linear parameters of the model. For example, in MRTM, the *DVR* parameter is the ratio of two linear parameters. This can produce bias in parameter values if the parameter in the denominator is noisy. Another arrangement of the linear equation has been proposed [69] so that *DVR* is one of the linear parameters

$$\int_0^t C_T(\tau)d\tau = DVR \int_0^t C_{Ref}(\tau)d\tau + \left(DVR/k'_2\right)C_{Ref}(t) - (1/k_2)C_T(t). \qquad (20)$$

The cost of this formulation, denoted LSRTM, is that noisier variables [$C_T(t)$ instead of $\int_0^t C_T(\tau)d\tau$] are used as the independent variables, which can introduce bias. One proposed strategy to reduce this bias is to use a clustering method to replace noisy single-voxel data terms in the independent variables by cluster-based terms [70]. This approach was proposed for (20) but may be also used for other (multi)linear methods.

A summary list of (most) methods that have been applied for parametric imaging with tracers that can be well fitted using the 1TC model is presented in Table II.

C. Direct Reconstruction of Parametric Images

In most studies, parametric images are computed by first reconstructing a series of frame images, and then applying kinetic modeling to each voxel TAC. This two-step approach is called the indirect method. Alternatively, the kinetic modeling can be applied directly within image reconstruction, which is referred to as direct reconstruction. The theoretical advantage of the direct approach is that the statistical properties of raw projection data are known, i.e., they follow the Poisson distribution, while the statistical properties of reconstructed frame images are not well characterized, and thus the proper cost function cannot be defined when applying kinetic modeling to frame-based data. These direct reconstruction algorithms produce parametric images with lower variability at equivalent dose [71]–[75], and have thus been the focus of substantial research efforts in recent years.

The first challenge of the direct approach is to derive an algorithm that can effectively maximize a cost function, such as the likelihood function. The expectation-maximization (EM) algorithm has been used for decades for

emission image reconstruction based on the maximum likelihood principle [76]–[78]. Direct parametric reconstruction algorithms based on the EM algorithm have been proposed for specific kinetic models, such as the Patlak analysis [79]–[82], spectral analysis [83], and the 1TC model without [72], [84] or with [73], [85] blood volume correction, the relative equilibrium plot [86], [87], and the Logan graphical analysis [88]. These kinetic models correspond to two categories. In the first category, the kinetic model is a multilinear model, or a multilinear sum of predefined basis-functions [79]–[83], [86], [87]. For these multilinear models, update equations for parametric images are similar to the one used for reconstruction of activity images using the EM algorithm. For example, for the Patlak analysis, the EM update equation for the parameters K_i and V_E (here labeled K and V, for notational convenience) are

$$K_j^{(n+1)} = \frac{K_j^{(n)} \sum_{k,i} \frac{Y_{k,i}}{Y_{k,i}^{(n)}} c_{k,j} \int_0^{t_i} C_A(\tau) d\tau}{\sum_{k,i} c_{k,j} \int_0^{t_i} C_A(\tau) d\tau}$$

$$V_j^{(n+1)} = \frac{V_j^{(n)} \sum_{k,i} \frac{Y_{k,i}}{Y_{k,i}^{(n)}} c_{k,j} C_A(t_i)}{\sum_{k,i} c_{k,j} C_A(t_i)} \qquad (21)$$

which is similar to the update equation used to reconstruct activity images λ_i

$$\lambda_{j,i}^{(n+1)} = \frac{\lambda_{j,i}^{(n)} \sum_k \frac{Y_{k,i}}{Y_{k,i}^{(n)}} c_{k,j}}{\sum_k c_{k,j}} \qquad (22)$$

where the indices i, j, k, and (n) are used for time points, voxels, lines of response (or sinogram bins), and iteration numbers, respectively, and the coefficient $c_{k,j}$ are the elements of the scanner system matrix (probability of observing an event from voxel j in line of response k), $Y_{k,i}$. are the counts observed in line of response k at time index i, and $Y_{k,i}^{(n)}$ are the expected counts at the nth iteration from line of response k at time index i. In short, for these linear models, the sum over the line-of-response index k in (22) is expanded to include the time point index i (21), and the coefficients $c_{k,j}$ of the system matrix are scaled by the independent variables corresponding to each linear parameter. It should be noted that the convergence properties of some of these algorithms can be nonoptimal (e.g., slow) and also tracer-dependent. For example, the direct EM algorithm for the Patlak plot converges very slowly for ^{18}F-FDG data [82].

In the second category of kinetic models for which an EM solution was proposed, the kinetic model contains a nonlinear term that is a convolution of the input function with an exponential function [72], [73], [84], [85], [88], which is a usual property of compartmental models used in PET. As for the linear algorithms above, these algorithms propose one-step update equations for all parameters. The update equations for linear parameters, e.g., (21) and (22), are multiplicative, so all parameter values are non-negative since all terms in the update are non-negative. The update equation for the nonlinear parameter is not multiplicative, and can be implemented using look-up table(s) precomputed using the input function curve only, if motion correction is not included [72], or the

TABLE II
LIST OF METHODS USED FOR TRACERS USING THE 1TC MODEL

METHOD	EQUATION	REFS
1TC	$C_T(t) = K_1 C_A(t) \otimes e^{-k_2 t}$	[9]
Logan Graphical Analysis*#	$\dfrac{\int_0^t C_T(\tau) d\tau}{C_T(t)} = V_T \dfrac{\int_0^t C_A(\tau) d\tau}{C_T(t)} + b, \quad t \geq 0$	[33]
Linearized 1TC§	$C_T(t) = K_1 \int_0^t C_A(\tau) d\tau - k_2 \int_0^t C_T(\tau) d\tau$	[66]
MA1*#§	$C_T(t_i) = -\dfrac{V_T}{b} \int_0^t C_A(\tau) d\tau + \dfrac{1}{b} \int_0^t C_T(\tau) d\tau$	[58]
LEGA*#	$Z_i^* = \dfrac{\sum_{j=1}^{i-1} Z_j^* d_j + \frac{1}{8} Z_{i-1}^* d_i - V_T \int_0^{t_i} C_a(\tau) d\tau}{b - \frac{3}{8} d_i}$	[63]
GLLS$		[67]
SRTM	$C_T(t) = R_1 C_{Ref}(t) + R_1 (k_2' - k_2) C_{Ref}(t) \otimes e^{-k_2 t}$	[28],[62]
Logan Reference Graphical Analysis**	$\dfrac{\int_0^t C_T(\tau) d\tau}{C_T(t)} = DVR \dfrac{\int_0^t C_{Ref}(\tau) d\tau}{C_T(t)} + b'', \quad t > t^*$	[34]
Logan Reference Graphical Analysis*#	$\dfrac{\int_0^t C_T(\tau) d\tau}{C_T(t)} = DVR \dfrac{\int_0^t C_{Ref}(\tau) d\tau + C_{Ref}(t)/k_2'}{C_T(t)} + b, \quad t \geq 0$	[34]
MRTM*#	$C_T(t_i) = -\dfrac{DVR}{b} \left\{ \int_0^t C_{Ref}(\tau) d\tau + C_{Ref}(t_i)/k_2' \right\} + \dfrac{1}{b} \int_0^t C_T(\tau) d\tau$	[59]
LSRTM	$\int_0^t C_T(\tau) d\tau = DVR \int_0^t C_{Ref}(\tau) d\tau + (DVR/k_2') C_{Ref}(t) - (1/k_2) C_T(t)$	[69]

* When a tracer can be fitted with the 1TC model, t^*=0

\# When a tracer can be fitted with the 1TC model, b=-1/k_2.

§ Linearized 1TC and MA1 are identical method when t^*=0, used in different contexts: estimation of blood flow and receptors studies, respectively.

$ Equations omitted due the multistep, iterative nature of GLLS, and space constraints.

** Even when a tracer can be fitted with the 1TC model, t^* is not guaranteed to be 0 for this version of the Logan reference graphical analysis

input function curve and the time-varying system matrix, when motion correction is included [84].

Alternatively, general frameworks, which could be applied to several models, have been proposed to separate the tomographic (spatial) parts of the reconstruction algorithm from the kinetic (temporal) modeling parts [74], [89], [90]. These general frameworks were developed to: 1) propose less kinetic-model-specific reconstruction algorithms and 2) increase the computation speed of the reconstruction algorithms compared to some of the aforementioned model-specific EM algorithms, in particular for ^{18}F-FDG Patlak direct reconstruction [90]. These general algorithms are sometimes described as nested algorithms, especially for linear models, since they are using two nested loops of iterations to maximize the likelihood function. The outer loop includes the tomographic projection steps and is not model specific (see [90, eq. (17)], [74, eq. (12)], or [89, eq. (41)]). The inner loop maximizes an objective function in image space, where all voxels are independent. Different solutions have been proposed for this inner loop, depending whether the kinetic model is linear [90] or nonlinear [74]. The inner loop is less computationally expensive, especially for linear models, than the outer loop and several inner-loop iterations may be performed per outer-step to reduce overall computation time [90].

The second challenge of the direct approach is that it must be compatible with motion correction. All the algorithms described in this section are amendable, if motion information is known, since using a time-variant system matrix $c_{k,j,i}$ is possible [84], [89], [91]. Information about motion may be obtained using a tracking device [92], especially for brain studies, or estimated from analysis of raw PET data, tracking device information, and/or frame images (see Section III-C). Alternatively, direct reconstruction may incorporate data-driven motion estimation and correction in the maximization of the likelihood function [93].

The third challenge for the direct approach is that the relevant model to apply may be only known for the tissue(s) of interest, but not surrounding tissues present in the field of view of the scanner. If the applied kinetic model cannot fit correctly these surrounding tissues, errors could propagate to the tissue of interest [94]. One approach is to apply the kinetic model only in the organ(s) of interest, and apply nonphysiological but more flexible models, such as splines, elsewhere [95], [96].

Finally, although the direct approach can provide parametric images with lower variability at equivalent dose than the matching indirect approaches, this improvement may not be enough by itself if the resulting parametric image noise is too high, and regularization or smoothing of the data may still be required. Direct reconstruction algorithms incorporating regularization have already been proposed, e.g., [74], [97], and [98] but further development is needed in this area, as well as well as more comparison of the performance of the direct versus indirect approach, with the best noise-reduction method applied to each approach.

Direct reconstruction will not eliminate the need for frame-based reconstruction, since frame-based data is still useful and more convenient to provide information needed to prepare input function data (e.g., to apply a global delay or dispersion correction to arterial input sample data) or prior information (e.g., to coregister to a MR or CT image) into the direct reconstruction algorithm. Moreover, for kinetic models using a reference region, most direct reconstruction approach assumes that the reference region TAC to be used for input in the kinetic model is already known: i.e., it has been computed from a previous reconstructed series of frame images. Alternatively, the computation of the reference region TAC can be incorporated in the direct reconstruction [71] if the location of the reference region is known.

III. CHALLENGES IN PARAMETRIC IMAGING

A. Input Functions

1) Traditional Input Function Measurement: Computation of parametric images requires the measurement of the model input function. Unless a reference region can be used, this is conventionally obtained via arterial cannulation, centrifugation of blood samples (to get plasma concentration), and in most cases, analysis of the plasma for radiolabeled metabolites by high-performance liquid chromatography (HPLC). Arterial cannulation is a cumbersome procedure and requires additional personnel and equipment. It also makes it more difficult to recruit subjects (healthy controls and patients) for clinical research.

2) Metabolite Correction: Radiometabolites can be observed in arterial plasma for almost all tracers, expect for a few such as ^{18}F-FDG. For brain studies, since the blood-brain barrier inhibits radiometabolites from entering into brain tissue (otherwise the radiotracer is considered as poor and most often abandoned), radiometabolite contribution should be removed from the measured plasma radioactivity. For other organs, since metabolites may contribute to the PET or SPECT tissue signal and have different kinetic properties, metabolites should ideally be treated separately in the kinetic model if they enter the tissues of interest. The percentage of unchanged tracer (parent fraction) is typically measured using HPLC analysis of several arterial plasma blood samples. Empirical functions (e.g., sums of exponentials or sigmoidal functions; for review, see [99]) are applied for curve fitting to obtain a continuous unchanged parent fraction curve. See Fig. 6 for examples of parent fraction curves for three different tracers. The product of the measured total plasma curve and the unchanged parent fraction curve is the final input function. This procedure is called metabolite correction.

Metabolite correction is applied to the input function, under the assumption that only the parent tracer enters the tissue of interest. For brain studies, radiotracers are usually selected during development not to have metabolites entering in the imaged tissue, by taking advantage of the properties of the blood-brain barrier. In other organs without blood-tissue barrier, such selection is harder. If metabolites do enter the imaged tissue, accurate quantification becomes more challenging, requiring models taking into account both parent tracer and its metabolites and their respective input (dual-input models) [100]–[106]. However, the parameters of these models are usually much harder to estimate reliably, and validation of the results is difficult or impossible since it would require invasive sampling of the imaged tissue. To the best of our knowledge, such models have only been used for ROI TAC analyses, but not parametric imaging.

Additional corrections may be needed for the input function data. First, delay [66], [107]–[109] and dispersion [109], [110] correction may be needed since the sampling point (typically a radial artery in humans) could be further away from the heart than the imaged tissue. Additional external delay and dispersion could also be introduced by the sampling device itself, especially with automated blood counter or samplers [111], [112]. Finally, if plasma is not directly measured, but only whole blood activity is measured (as is typical with automated blood counters), then a correction for the plasma to whole blood ratio is also needed. Differences between plasma and whole blood values may be due to: 1) tracers that do not enter blood cells; 2) slow exchanges between the plasma and blood cells for the parent tracer and/or its metabolites; or 3) differences in uptake into the blood cells between the tracer and its metabolites [9], [113], [114].

3) Image-Derived Input Function: As a noninvasive alternative to arterial blood sampling, many image-derived input function (IDIF) methods have been proposed to

either: 1) reduce the number of arterial samples or 2) to obviate the need for arterial blood sampling at all. IDIFs take advantage of the radioactivity in the blood vessels in the dynamic PET images to estimate the input function. Note that IDIF methods only estimate the radioactivity in the whole blood, since it cannot differentiate the plasma radioactivity from whole blood radioactivity, nor can it differentiate parent tracer from radiometabolites. Thus, blood sampling may still be required for metabolite correction for many tracers, unless a predetermined population-based metabolite correction can be used. Moreover, manual ROI delineation is time consuming, labor intensive, and operator dependent [115]. IDIF methods tend to be more successful for cardiac imaging than for brain studies, since the left ventricle or aorta are larger and easier to segment, compared with the carotid artery. Also, other modalities (MR and CT) are more promising to be used for extraction blood pools, if available [116]–[119].

Many IDIF methods have been proposed for brain studies. Since the available intracranial blood vessels in the field of view are the carotid arteries with an average diameter of $\sim$4–6 mm [120], [121], this is challenging for PET scanners with spatial resolution of $\sim$6 mm because of the partial volume effect. Eight existing IDIF methods for these PET scanners were evaluated for ^{18}F-FDG brain PET data [122]. Among these, the more invasive methods (i.e., using blood samples to scale the estimated input function, and/or provide partial volume correction for the blood ROI [123]) provided excellent results for MR$_{\text{glu}}$ estimation. The simulation and clinical data suggested that a reliable, and completely blood-sample free, procedure was not available [124]. On the other hand, IDIF methods are more promising in whole body scans since large blood pools are available. The left ventricle, left atrium, and the ascending/descending/abdominal aorta have been used to estimate input curves [125]–[129]. Since the PET scan framing is not typically frequent enough to capture the early peak of the input function, the IDIF-derived input functions are less suitable for the estimation of micro-parameters (K_1, k_2, k_3, and k_4), since these are more susceptible to bias if there are errors in the shape of the early portion of the input function. On the other hand, macro-parameters, such as K_i and V_T, estimated with graphical analysis methods (Patlak and Logan, see above) only depend on the integral of the input curve before t^*. Since accurate measurement of the area under the curve does not require rapid sampling, graphical analysis methods are more compatible with IDIFs than nonlinear compartment model analysis.

Subject head, body, and respiratory motion (RM) will affect the shape of the IDIF input function. Since high uptake in the blood pool is usually seen in the early portion of a dynamic PET study, regions of interest are typically defined on the early summed images. When patient motion occurs, the ROIs and the target blood pools become mismatched at later frames. In some studies, it was observed that scaling or correcting the IDIF using late blood samples reduced vulnerability to motion [130]. Moreover, patient motion affects not only the IDIF estimation but also the measurement of the TAC of each voxel. Therefore, motion correction is particularly important for parametric analysis (see Section III-C).
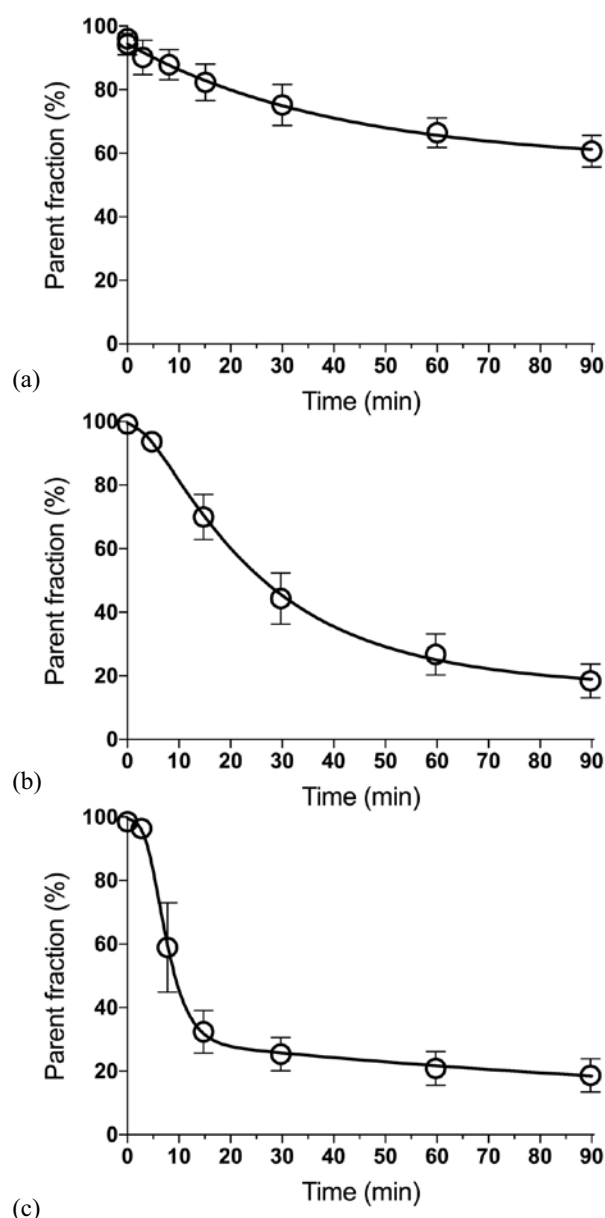

Fig. 6. Samples metabolite curves. Mean $\pm$ SD of parent fraction in the plasma after injection of (a) ^{11}C-LNS-3172176 ($n = 12$), a muscarinic type 1 receptor ligand, (b) ^{11}C-LY2795050 ($n = 16$), a κ-opioid receptor ligand, and (c) ^{18}F-MK-6577 ($n = 13$), a glycine transporter 1 ligand. Data in (a) were fitted with a single exponential function (two fitted parameters), data in parts (b) and (c) were fitted to a sigmoid function (four fitted parameters).

4) Population-Based Input Function: An alternative to the IDIF method is a population-based input function (PBIF) method. PBIFs assume that there is a common shape (template) of input functions among subjects. The method generates a template shape of input function using normalized individually measured input functions, and then scales the template input function for use. The PBIF method has been mainly validated in ^{18}F-FDG studies [131]–[136]. The calibration values were taken from various parameters [arterial blood samples, arterialized venous samples, administered activity (AA), body weight, and blood transit time, or AA and body surface area, and cerebellum TAC]. Since PBIFs do not use dynamic

PET images, the PBIF-derived input function is not affected by partial volume effects and patient motion. For example, the shape of the early peak part of the input function is generally more plausible than the IDIF input function [124]. However, an important limitation of the PBIF method is that the shape of the input function can be different between subject groups (healthy controls, patients, and before and after treatment), between subjects in the same group, or even within the same subject between baseline and post-treatment scans [137].

5) Metabolite Fraction Correction for IDIFs and PBIFs: For most radiotracers, radiometabolite contribution should be excluded from the IDIF-derived or population input functions. Since the change of parent fraction over time can vary between individual subjects or between groups with different conditions, application of a population-based unchanged tracer curve to the estimated total input function may not be an accurate solution to exclude radiometabolites contribution, so such an approach requires careful validation. This is especially true for tracers with very low parent fraction at late times, where small differences in the parent fractions can cause large errors in the parameter estimates. Similarly, correction for the plasma to whole blood ratio may be needed too. Again, a population-based correction could be used if intersubject variability is low or correction is minor (e.g., for ^{18}F-FDG [123], [138]); alternatively, the correction can be based on the subject's hematocrit (from tracers not entering blood cells at all), or since changes in the plasma to whole blood ratio during the scan can be due to tracer metabolism, the plasma to whole blood correction may be inferred from the metabolite correction data [9], [113], [114].

6) Simultaneous Estimation of the Input Function: Another alternative to the IDIF method is a simultaneous estimation (SIME) approach. This method's goal is to estimate the input function simultaneously with the kinetic parameters from several ROIs. The input function is assumed to be common to all ROIs and is described by an analytical function with parameters that are incorporated into the objective function to be optimized by fitting data from several ROIs simultaneously [139]. This approach theoretically allows us to estimate the metabolite-corrected input function. However, there is a large number of parameters to be optimized, and the shape of the cost function may not be convex, and thus careful validation is required for each tracer. Moreover, at least one blood sample is needed to determine the scaling factor for the input function [139].

B. Noise Reduction Algorithms

It is rare to be able to perform parametric imaging without some form of noise reduction due to the high level of noise in single-voxel TACs. Noise reduction can be done in the temporal and/or spatial domains. If done carefully, these algorithms can produce significant noise reduction with minimal loss of accuracy. However, in general, such methods must be tuned and validated for each imaging and analysis situation.

For spatial approaches, Gaussian smoothing is one of the simplest methods to reduce noise in the original dynamic images before applying kinetic analysis, at the cost of lowered resolution. One method to preserve boundaries between adjacent regions with different kinetics is to use the bilateral filter [140]: in a Gaussian filter, a filtered image is computed using a Gaussian kernel taking into account only the distance of neighboring voxels; in a bilateral filter, the kernel also takes into account the difference in intensities between neighboring voxels, reducing the weight of neighboring voxels with very different intensities in the unfiltered image, which helps to preserve edges in the input image; to filter dynamic datasets, the L2 norm over all frames intensities can be used to apply a consistent filter for all frames. Another method for brain cortical regions is to perform smoothing along the surface of the cortex [141], using segmentation information from an MR image, to avoid mixing gray matter signals with white matter or cerebrospinal fluid signals.

Wavelet transforms applied in the spatial domain have been used to reduce noise in PET parametric images while preserving resolution [142]–[146], since wavelets can represent signals which are localized in both time (or space) and frequency. Wavelets can be used to smooth the images before applying the kinetic model, or since wavelet transforms are linear operators, a linear kinetic model can be applied in wavelet space and transformed back to the original image space [145].

In the temporal domain, one of the easiest ways to reduce noise is to limit the range of the basis functions used in models such as the 1TC and SRTM models. For tracers with favorably fast kinetics, it is possible to limit basis functions by using a higher value for the lower limit on the range of the k_2 values used to precompute the basis functions, based on empirical knowledge from previous studies or from analyses of regional TACs [68], [147]. This method reduces outlier V_T values associated with low k_2 values when the shape of the cost function is relatively flat for low k_2 values. If feasible, this simple approach can allow computation of parametric images without smoothing, i.e., at the original resolution of the input dynamic images data. Wavelets can also be used to filter PET data in the temporal domain [11], [148], in particular in multiple-injection studies were the ability of wavelets to preserve sharp localized (in time) features is particularly important [11].

Principal component analysis (PCA) is a data reduction method that can be used to reduce the noise in individual voxel TACs before applying kinetic modeling [149]–[153]. This approach maintains the kinetic profiles that linearly contribute a large fraction of the variance of the data. Related methods such as factor analysis and independent component analysis can also be used to reduce the noise in PET data, though they are more frequently used to extract or separate signals such as the input function and tissue curves [152], [154], [155] in cardiac studies. PCA denoising has the advantage of preserving spatial resolution, however it can also introduce biases if there are small regions with atypical kinetics which are not retained in the selected principal components, i.e., if the fraction of total data variance produced by these regions is small.

Finally, other methods apply combined spatio-temporal smoothing. One such method, called highly constrained

backprojection—local reconstruction (HYPR-LR) originated from the field of magnetic resonance image reconstruction [156] and has been adapted to PET denoising [157], [158] and image reconstruction [159]. In this method, a lower noise composite image, obtained by summing image frames over a long time-interval, is used to help reduce noise without sacrificing resolution. In the first implementation, the composite image was computed using the sum of all PET data, but this introduced biases since the composite image should have the same contrast as each noisy frame image, while this contrast typically changes over time in the dynamic data. Therefore, a second implementation was proposed using several, shorter, composite images for different phases of the study [158]. This reduced the aforementioned bias at the cost of less noise reduction. The HYPR algorithm belongs to the family of guided image filtering [160], [161]. Such algorithms were also used on the dynamic sinogram data, before reconstruction, using the sum sinogram for the whole dynamic scan to denoise individual frame sinograms [162].

Methods that smooth the imaging data in the temporal domain (PCA and HYPR) produce frame images which are no longer uncorrelated. When kinetic analysis is then applied using (weighted) least squares, this leads to violations of the assumptions of the least squares method. Furthermore, the appropriate weights, if any, to use after smoothing are also more complicated to determine. The practical impact of these issues is typically low since the remaining level of noise is low in the filtered images, but has not been investigated to the best of our knowledge.

Instead of presmoothing or filtering the PET data, another strategy is to apply regularization during the computation of the parametric maps. One family of algorithms is based on ridge regression, where a penalty term is added to the usual weighted least square cost function

$$\mathbf{\Psi} = \sum_i w_i \big(C_{\text{PET}}(t_i) - C_{\text{T}}(t_i, \theta)\big)^2 + \beta \sum_j \alpha_i \big(\theta_j - \mu_j\big)^2$$

(23)

where i is the index on image frames, j is the index on the parameter array θ, C_{PET} is the measured data, and C_{T} is the model prediction; μ is a vector of *a priori* values for θ, w and α are vectors of weights for C_{PET} and μ, respectively, and β is a global weight factor for the penalty term (a hyperparameter). In a Bayesian framework, the second term in (23) can be generalized using the *a priori* covariance matrix of the parameters

$$\mathbf{\Psi} = (\mathbf{C}_{\text{PET}} - \mathbf{C}_T)^t \mathbf{\Sigma}_{\text{PET}}^{-1}(\mathbf{C}_{\text{PET}} - \mathbf{C}_T)$$
$$+ (\boldsymbol{\theta} - \boldsymbol{\mu})^t \mathbf{\Sigma}_{\boldsymbol{\theta}}^{-1}(\boldsymbol{\theta} - \boldsymbol{\mu})$$

(24)

where $\mathbf{\Sigma}_{\text{PET}}$ and $\mathbf{\Sigma}_{\boldsymbol{\theta}}$ are the covariance matrices of the PET measurement errors and the *a priori* information on the parameters, respectively. Knowledge of α, μ, and β (or $\mathbf{\Sigma}_{\text{PET}}$ and $\mathbf{\Sigma}_{\boldsymbol{\theta}}$) is needed and this knowledge can be inferred from several sources. In one category of algorithms, this knowledge is inferred from a population of subjects previously or concurrently analyzed [163]–[166]. In another category

of algorithms, this knowledge is inferred from the current dynamic image set where the population of subjects can be replaced by a population of voxels, selected by a clustering algorithm [167], [168], or alternatively, the *a priori* knowledge can be inferred for each voxel from neighboring voxels. In these algorithms, μ and α can be inferred from the results of a first pass of unconstrained weighted least square fits, and cluster-based or locally applied statistical functions [69], [169]. Alternatively, α, μ, and β may be estimated in a hierarchical fashion using regional TACs with lower noise [170].

The weights α and β (or $\mathbf{\Sigma}_{\text{PET}}$ and $\mathbf{\Sigma}_{\boldsymbol{\theta}}$) control the strength of a priori knowledge of μ. In some algorithms, these weights are automatically determined as part of the procedure [69], [169], [171]. In other algorithms, the scaling parameter β is optimized in a separate analysis [163], [164].

For linear models, an analytical solution is readily available to minimize the cost functions in (23) or (24) [164], [169]. For example, using the notations in (12) and (24), the maximum *a posteriori* solution is given by

$$\boldsymbol{\beta} = \left(\mathbf{X}^t \mathbf{\Sigma}_{\text{PET}}^{-1} \mathbf{X} + \mathbf{\Sigma}_{\boldsymbol{\theta}}^{-1}\right)^{-1} \left(\mathbf{X}^t \mathbf{\Sigma}_{\text{PET}}^{-1} \mathbf{C}_{\text{PET}} + \mathbf{\Sigma}_{\boldsymbol{\theta}}^{-1} \boldsymbol{\mu}\right). \quad (25)$$

For nonlinear models, modified iterative fitting algorithm can be used [171]. For this reason, traditionally nonlinear models like the 1TC model or the SRTM can be linearized [69], even though the linear implementation of these models suffers from bias induced by noise in the independent variables. To further mitigate the biases introduced by these noisy independent variables, one strategy is to use a clustering method to replace noisy single-voxel data terms in the independent variables by cluster-based terms [70].

Another way to implement regularization is to share one parameter across all voxels. We previously introduced the MRTM2 and SRTM2 methods, which regularize the MRTM and SRTM methods, respectively, by estimating only one value per scan, instead of one value per voxel, of k_2', a parameter linked to the reference region TAC only. Similarly, some authors have proposed to share across all voxels specific model parameters, in this case based on physiological assumptions. For example, it was proposed to share the parameter k_4 of FRTM in receptor studies [172]. The parameter k_4 could be uniform if one assumes that this parameter only depends on the properties of the radioligand, and not on the local tissue properties (i.e., if the model assumptions are accurate and k_4 is truly equal to the tracer's dissociation rate k_{off}).

C. Motion Correction

Patient motion is a well-known and ever-present cause of artifacts in PET imaging. Based on the physiological cause and anatomy, patient motions can be divided into RM [173], head motion (HM) [174]–[176], body torso motion (BM) [174], cardiac motion (CM) [173], [177], and other motions, e.g., bowel motion [178]. Here, we focus on RM, HM, BM, and CM. Periodic RM causes organs to move up to 25 mm [179] between end-expiration and end-inspiration phases, mostly in the superior-inferior and anterior-posterior directions. Cardiac movement is $\sim$13 mm along the long axis and $\sim$7 mm
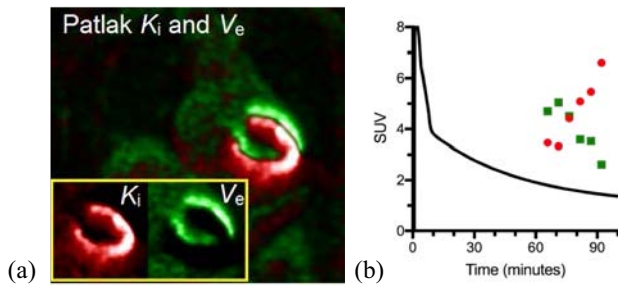
Fig. 7. ^{18}F-FDG whole-body direct parametric reconstruction (40–90 min since injection). (a) Mismatch between the K_i (red) image and the V_E (green) image was introduced by respiratory baseline shift. (b) Voxels initially in the ventricle (red) for the first two passes were located later in the myocardium, producing artifactly high K_i and low V_E values, while voxels initially in the myocardium (green), were located outside later, leading to artifactly high V_E and low K_i values.

for the mid left ventricle between end diastole and end systole [180]. Comparing to periodic RM and CM, the timing for HM or BM is unpredictable. In general, the longer scans needed for parametric imaging lead to higher likelihood and higher amplitude of HM and BM [175], [176], [181] with accompanying higher probability to observe variations in RM.

1) PET and CT Mismatch: If a breath-hold CT is used, the CT image is a snapshot of one respiratory phase, while PET images are an average over all breathing phases and cycles. This mismatch can lead to attenuation correction (AC) artifacts [179], [182], especially at the boundary of organs with large attenuation differences, e.g., between lungs and liver or heart. Such artifacts can cause under- or over-estimation of tracer uptake [179], [183]. BM and HM can also cause similar AC artifacts when motion occurs between the CT (or transmission scan) and PET scans or during the PET scan. Motion can cause not only under-estimation but also over-estimation of kinetic parameters [184], [185]. An example of RM-induced mislocalization and over-estimation of myocardium K_i map is shown in Fig. 7. Due to the respiratory pattern change, the baseline of the heart shifted toward the inferior direction while scanning, which caused a mismatch-pattern between the K_i (red) and V_E (green) images.

2) Existing Respiratory Motion Correction Techniques: A variety of methods [186] using external devices have been proposed to track RM, including pressure monitoring, fiducial marker tracking, etc. This tracking produces 1-D respiratory surrogate traces that can be used for respiratory gating or motion correction. Alternatively, data-driven approaches, extracting the respiratory trace directly from PET raw data, have been proposed [187]–[195]. The data-driven approach is attractive since it does not require attachment of a tool to the subject. Respiratory gating, the rebinning the PET raw listmode data based on the respiratory phases, has been well studied [187]–[192], [194], [196]–[198] and implemented by manufacturers [199]. Using only part of the total counts, the main drawback of gating, will result in noisier images; this is especially damaging for parametric imaging, which already tends to produce more noisy

images than static imaging. On the other hand, RM correction (RMC) [200]–[218] can overcome such drawback by utilizing all the counts. RMC includes two subcategories: 1) post-reconstruction registration (PRR) [202], [213], [214], [219] and 2) motion-compensated image reconstruction (MCIR) [201], [203]–[208], [211], [212], [215], [216]. PRR typically nonrigidly registers all the respiratory gated images to a reference image. MCIR incorporates the RM information, typically generated through PRR, into the reconstruction system matrix to perform motion-corrected reconstruction. However, neither PRR nor MCIR corrects intragate motion or intercycle variation, which would yield suboptimal respiratory correction performance, especially for irregular breathers [220]. Recently, an internal–external (INTEX) correlation technique were proposed [179], [184], [193], [221], [222], which builds a correlation between an external respiratory trace and the movement of each image voxel (internal). INTEX yields a continuous temporal relationship between the external trace and each voxel's motion. Paired with the list-mode reconstruction [92], event-by-event RM can be achieved, and it corrects for intragate motion and intercycle variation, which overcomes the drawback of MCIR. On a PET/MR system, RM can be tracked using special MR sequences [223]–[228]. These MR sequences can directly allow to estimate a 3-D nonrigid motion field independently of the PET data, and these motion fields can then be used either post-reconstruction or during reconstruction (for review, see [229]–[231]). The motion information obtained from MR can be superior to the one obtained from PET since: 1) MR image quality is constant over time while PET image quality may be poor at the beginning of the scan, before the radiotracer distributes in all tissues, or at the end of the scan due to low counting statistics or 2) some MR sequences like tagged MRI provide detailed motion information within organs which are homogeneous from the PET signal point of view [225], [227]. The limitations of PET/MR motion correction are: 1) the lower availability of PE/MR scanners and 2) opportunity costs, i.e., the desire to use these PET/MR scanners to run other, non-notion related, MR sequences during the PET scan to obtain more interesting anatomical or functional information instead. To reduce motion-related MR sequence time, full motion information may be acquired for only part of PET scan, and then shorter MR sequences may be used to track the respiratory phase only, assuming the motion model built with the first sequences is valid throughout the PET scan [224].

3) Existing Head and Body Motion Management Approaches: For HM, physical constraints are often used to prevent HM [174]–[176], [232]. If motion happened during the scan, HM correction methods are needed [206], [233]–[247]. Typical HM correction involves two steps: motion detection and motion correction. For detection, external devices, such as Polaris Vicra optical tracking [236], [247], are often used. Such devices are usually robust but required careful setup and attachments to the patients. As for RM, on a PET/MR system HM can be tracked using MR sequences [230], [248] but there are fewer PET/MR systems than PET/CT systems. To overcome these drawbacks, some groups have proposed data-driven approaches [244], [249], [250], based on PET
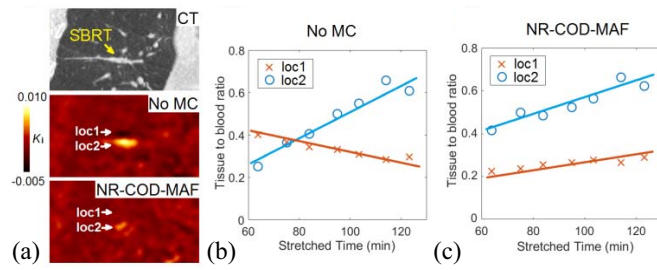
Fig. 8. Body motion impact on Patlak K_i estimations for an ^{18}F-FDG study. (a) Zoom-in region of the post-SBRT location, CT and K_i images are shown. (b) ROI-based Patlak plot for no motion correction. (c) Same as (b), but for body motion correction. Reproduced from Lu *et al.*, "Data-driven voluntary body motion detection and nonrigid event-by-event correction for static and dynamic PET," *Phys. Med. Biol.*, vol. 64, no. 6, 2019, Art. no. 065002. doi: 10.1088/1361-6560/ab02c2. Institute of Physics and Engineering in Medicine. Reproduced by permission of IOP Publishing. All rights reserved.

raw data itself, to detect head or body motions. For correction, PRR [251] is the simplest approach, which registers predefined dynamic-frame reconstructions to a reference frame. PRR, however, cannot correct for intraframe motions, motions happened inside one dynamic frame. Multiacquisition-frame (MAF) is a more accurate method used by many groups [234], [236], [240], [244]. In MAF, reconstructions without AC are performed for frames selected between the detected motion time points ("motion-free" frames), followed by image registrations between the motion-free frames to estimate the motions, which will be used in the final motion corrected reconstruction. Comparing HM, BM has been largely under-explored for PET. In addition, BM is nonrigid, where the correction is harder than the rigid HM. Nevertheless, studies [183], [252] have shown that for dynamic studies, BM can cause under- and over-estimation of kinetic parameters. An example of BM caused false-positive in terms of nodule malignancy is shown in Fig. 8, the location of the nodule shifted from location 1 to location 2 during the scan, which caused overestimated K_i for location 2 and negative K_i estimate for location 1. After motion correction, the K_i of location 2 became much closer to the value of the lung background, which indicated negative in terms of malignancy. Instead of correcting motion during the reconstruction, "precorrection" methods have also been proposed by some groups [233], [237]–[240], [253]–[256]. Such method rebins each line-of-response during the sinogram-generation step based on the motion estimate. In this method, normalization has to be carefully addressed [237], [238], [253], [255]–[257]. The precorrection approach only applies to rigid motion correction.

IV. CONCLUSION

The goal of parametric imaging for PET and SPECT studies is to create the most quantitatively accurate maps for the physiological target(s) of the study, by applying the proper modeling for the tracer kinetics at all voxels of image. Accurate parametric imaging requires to apply all appropriate corrections to the original dynamic imaging data, and in particular motion correction; to measure the correct input function for the radiotracer; and to apply a valid model for selected tracer and the

most suitable strategy to handle the typically high noise level observed at the single voxel level. All of these challenges are a function of the tracer and organ of interest, and may also be influenced by the study constraints and design or the scanner being used, and thus evaluation of the most appropriate methods is to be done per tracer or per study. Methodological improvements, either new enhanced methods or broader distribution of existing good-performance methods, are still needed at all steps of the process.

REFERENCES

[1] R. S. Frackowiak, G. L. Lenzi, T. Jones, and J. D. Heather, "Quantitative measurement of regional cerebral blood flow and oxygen metabolism in man using 15O and positron emission tomography: Theory, procedure, and normal values," *J. Comput. Assisted Tomography*, vol. 4, no. 6, pp. 727–736, Dec. 1980.

[2] M. E. Phelps *et al.*, "Tomographic measurement of local cerebral glucose metabolic rate in humans with (F-18)2-fluoro-2-deoxy-D-glucose: Validation of method," *Ann. Neurol.*, vol. 6, no. 5, pp. 371–388, Nov. 1979.

[3] E. S. Garnett, G. Firnau, and C. Nahmias, "Dopamine visualized in the basal ganglia of living man," *Nature*, vol. 305, no. 5930, pp. 137–138, Sep. 1983.

[4] M. A. Mintun, M. E. Raichle, M. R. Kilbourn, G. F. Wooten, and M. J. Welch, "A quantitative model for the in vivo assessment of drug binding sites with positron emission tomography," *Ann. Neurol.*, vol. 15, no. 3, pp. 217–227, 1984.

[5] J. S. Rasey, W.-J. Koh, J. R. Grierson, Z. Grunbaum, and K. A. Krohn, "Radiolabeled fluoromisonidazole as an imaging agent for tumor hypoxia," *Int. J. Radiat. Oncol. Biol. Phys.*, vol. 17, no. 5, pp. 985–991, 1989.

[6] E. M. Renkin, "Transport of potassium-42 from blood to tissue in isolated mammalian skeletal muscles," *Amer. J. Physiol.*, vol. 197, pp. 1205–1210, Dec. 1959.

[7] P. Herrero, J. Markham, M. E. Shelton, C. J. Weinheimer, and S. R. Bergmann, "Noninvasive quantification of regional myocardial perfusion with rubidium-82 and positron emission tomography. Exploration of a mathematical model," *Circulation*, vol. 82, no. 4, pp. 1377–1386, Oct. 1990.

[8] R. B. Innis *et al.*, "Consensus nomenclature for in vivo imaging of reversibly binding radioligands," *J. Cerebr. Blood Flow Metab.*, vol. 27, no. 9, pp. 1533–1539, Sep. 2007.

[9] R. N. Gunn, S. R. Gunn, and V. J. Cunningham, "Positron emission tomography compartmental models," *J. Cerebr. Blood Flow Metab.*, vol. 21, no. 6, pp. 635–652, Jul. 2001.

[10] P. Millet *et al.*, "Parameter and index images of benzodiazepine receptor concentration in the brain," *J. Nucl. Med.*, vol. 36, no. 8, pp. 1462–1471, Aug. 1995.

[11] P. Millet, V. Ibáñez, J. Delforge, S. Pappata, and J. Guimón, "Wavelet analysis of dynamic PET data: Application to the parametric imaging of benzodiazepine receptor concentration," *Neuroimage*, vol. 11, no. 5, pp. 458–472, Jun. 2000.

[12] M. Naganawa *et al.*, "Tracer kinetic modeling of [(11)C]AFM, a new PET imaging agent for the serotonin transporter," *J. Cerebr. Blood Flow Metab.*, vol. 33, no. 12, pp. 1886–1896, Dec. 2013.

[13] K. Erlandsson, I. Buvat, P. H. Pretorius, B. A. Thomas, and B. F. Hutton, "A review of partial volume correction techniques for emission tomography and their applications in neurology, cardiology and oncology," *Phys. Med. Biol.*, vol. 57, no. 21, pp. R119–R159, Nov. 2012.

[14] R. S. J. Frackowiak, K. J. Friston, R. J. Frith, and J. C. Mazziotta, Eds., *Human Brain Function*. San Diego, CA, USA: Academic, 1997.

[15] L. Nummenmaa, L. Tuominen, and I. Hirvonen, "Simultaneous PET-MRI confirms that cerebral blood flow does not confound PET neuroreceptor activation studies," *ACS Chem. Neurosci.*, vol. 9, no. 2, pp. 159–161, Mar. 2018.

[16] C. Y. Sander and S. Hesse, "News and views on in-vivo imaging of neurotransmission using PET and MRI," *Quart. J. Nucl. Med. Mol. Imag.*, vol. 61, no. 4, pp. 414–428, Dec. 2017.

[17] T. Karjalainen *et al.*, "Dissociable roles of cerebral μ-opioid and type 2 dopamine receptors in vicarious pain: A combined PET-fMRI study," *Cerebr. Cortex*, vol. 27, no. 8, pp. 4257–4266, Aug. 2017.

[18] H. D. Hansen *et al.*, "Functional characterization of 5-HT1B receptor drugs in nonhuman primates using simultaneous PET-MR," *J. Neurosci.*, vol. 37, no. 44, pp. 10671–10678, Nov. 2017.

[19] C. Y. Sander, J. M. Hooker, C. Catana, B. R. Rosen, and J. B. Mandeville, "Imaging agonist-induced D2/D3 receptor desensitization and internalization in vivo with PET&MRI," *Neuropsychopharmacology*, vol. 41, no. 5, pp. 1427–1436, Apr. 2016.

[20] H.-Y. Wey *et al.*, "Simultaneous fMRI-PET of the opioidergic pain system in human brain," *Neuroimage*, vol. 102, no. 2, pp. 275–282, Nov. 2014.

[21] C. Y. Sander *et al.*, "Neurovascular coupling to D2/D3 dopamine receptor occupancy using simultaneous PET/functional MRI," *Proc. Nat. Acad. Sci. USA*, vol. 110, no. 27, pp. 11169–11174, Jul. 2013.

[22] R. E. Carson, "PET physiological measurements using constant infusion," *Nucl. Med. Biol.*, vol. 27, no. 7, pp. 657–660, Oct. 2000.

[23] R. E. Carson *et al.*, "Comparison of bolus and infusion methods for receptor quantitation: Application to [18F]cyclofoxy and positron emission tomography," *J. Cerebr. Blood Flow Metab.*, vol. 13, no. 1, pp. 24–42, Jan. 1993.

[24] J. A. Jacquez, *Compartmental Analysis in Biology and Medicine. Kinetics of Distribution of Tracer-Labeled Materials*. Amsterdam, The Netherlands: Elsevier, 1972.

[25] C. Cobelli and R. N. Bergman, *Carbohydrate Metabolism: Quantitative Physiology and Mathematical Modelling*. Chichester, U.K.: Wiley, 1981.

[26] J. A. Jacquez, *Compartmental Analysis in Biology and Medicine*, 2nd ed. Ann Arbor, MI, USA: Univ. Michigan Press, 1985.

[27] C. Cobelli, D. Foster, and G. Toffolo, *Tracer Kinetics in Biomedical Research: From Data to Model*. New York, NY, USA: Kluwer, 2000.

[28] A. A. Lammertsma and S. P. Hume, "Simplified reference tissue model for PET receptor studies," *Neuroimage*, vol. 4, no. 3, pp. 153–158, Dec. 1996.

[29] G. Blomqvist *et al.*, "Dynamic models for reversible ligand binding," in *Positron Emission Tomography in Clinical Research and Clinical Diagnosis*, C. Beckers, A. Goffinet, and A. Bol, Eds. Dordrecht, The Netherlands: Kluwer, 1989, pp. 35–44.

[30] V. J. Cunningham *et al.*, "Compartmental analysis of diprenorphine binding to opiate receptors in the rat in vivo and its comparison with equilibrium data in vitro," *J. Cerebr. Blood Flow Metab.*, vol. 11, no. 1, pp. 1–9, Feb. 1991.

[31] S. Hume *et al.*, "Quantitation of carbon-11-labeled raclopride in rat striatum using positron emission tomography," *Synapse*, vol. 12, no. 1, pp. 47–54, 1992.

[32] H. C. Watabe, R. E. Carson, and H. Iida, "The reference tissue model: Three compartments for the reference region," *Neuroimage*, vol. 11, no. 6, p. S2. 2000.

[33] J. Logan *et al.*, "Graphical analysis of reversible radioligand binding from time-activity measurements applied to [N-11C-methyl]-(-)-cocaine PET studies in human subjects," *J. Cerebr. Blood Flow Metab.*, vol. 10, no. 5, pp. 740–747, Sep. 1990.

[34] J. Logan *et al.*, "Distribution volume ratios without blood sampling from graphical analysis of PET data," *J. Cerebr. Blood Flow Metab.*, vol. 16, no. 5, pp. 834–840, Sep. 1996.

[35] R. N. Gunn, S. R. Gunn, F. E. Turkheimer, J. A. D. Aston, and V. J. Cunningham, "Positron emission tomography compartmental models: A basis pursuit strategy for kinetic modeling," *J. Cerebr. Blood Flow Metab.*, vol. 22, no. 12, pp. 1425–1439, Dec. 2002.

[36] M. Slifstein and M. Laruelle, "Effects of statistical noise on graphic analysis of PET neuroreceptor studies," *J. Nucl. Med.*, vol. 41, no. 12, pp. 2083–2088, Dec. 2000.

[37] E. Wallstén, J. Axelsson, M. Karlsson, K. Riklund, and A. Larsson, "A study of dynamic PET frame-binning on the reference Logan binding potential," *IEEE Trans. Radiat. Plasma Med. Sci.*, vol. 1, no. 2, pp. 128–135, Mar. 2017.

[38] J. V. Beck and K. J. Arnold, *Parameter Estimation in Engineering and Science*. New York, NY, USA: Wiley, 1977.

[39] C. S. Patlak, R. G. Blasberg, and J. D. Fenstermacher, "Graphical evaluation of blood-to-brain transfer constants from multiple-time uptake data," *J. Cerebr. Blood Flow Metab.*, vol. 3, no. 1, pp. 1–7, 1983.

[40] C. S. Patlak and R. G. Blasberg, "Graphical evaluation of blood-to-brain transfer constants from multiple-time uptake data. Generalizations," *J. Cerebr. Blood Flow Metab.*, vol. 5, no. 4, pp. 584–590, 1985.

[41] S. Okazumi *et al.*, "Evaluation of liver tumors using fluorine-18-fluorodeoxyglucose PET: Characterization of tumor and assessment of effect of treatment," *J. Nucl. Med.*, vol. 33, no. 3, pp. 333–339, Mar. 1992.

[42] T. Torizuka *et al.*, "In vivo assessment of glucose metabolism in hepatocellular carcinoma with FDG-PET," *J. Nucl. Med.*, vol. 36, no. 10, pp. 1811–1817, Oct. 1995.

[43] V. J. Cunningham and T. Jones, "Spectral analysis of dynamic PET studies," *J. Cerebr. Blood Flow Metab.*, vol. 13, no. 1, pp. 15–23, Feb. 1993.

[44] J. Delforge *et al.*, "Cardiac beta-adrenergic receptor density measured in vivo using PET, CGP 12177, and a new graphical method," *J. Nucl. Med.*, vol. 32, no. 4, pp. 739–748, May 1991.

[45] J. Delforge *et al.*, "Kinetic analysis of central [76Br]bromolisuride binding to dopamine D2 receptors studied by PET," *J. Cerebr. Blood Flow Metab.*, vol. 11, no. 6, pp. 914–925, Nov. 1991.

[46] E. D. Morris, N. M. Alpert, and A. J. Fischman, "Comparison of two compartmental models for describing receptor ligand kinetics and receptor availability in multiple injection PET studies," *J. Cerebr. Blood Flow Metab.*, vol. 16, no. 5, pp. 841–853, Sep. 1996.

[47] J. Delforge, A. Syrota, and B. M. Mazoyer, "Identifiability analysis and parameter identification of an in vivo ligand-receptor model from PET data," *IEEE Trans. Biomed. Eng.*, vol. 37, no. 7, pp. 653–661, Jul. 1990.

[48] J. Delforge *et al.*, "Modeling analysis of [11C]flumazenil kinetics studied by PET: Application to a critical study of the equilibrium approaches," *J. Cerebr. Blood Flow Metab.*, vol. 13, no. 3, pp. 454–468, Jun. 1993.

[49] L. Farde, H. Hall, E. Ehrin, and G. Sedvall, "Quantitative analysis of D2 dopamine receptor binding in the living human brain by PET," *Science*, vol. 231, no. 4735, pp. 258–261, Jan. 1986.

[50] J. E. Holden, S. Jivan, T. J. Ruth, and D. J. Doudet, "In vivo receptor assay with multiple ligand concentrations: An equilibrium approach," *J. Cerebr. Blood Flow Metab.*, vol. 22, no. 9, pp. 1132–1341, Sep. 2002.

[51] Y. Xia *et al.*, "Measurement of Bmax and Kd with the glycine transporter 1 radiotracer (1)(8) F-MK6577 using a novel multi-infusion paradigm," *J. Cerebr. Blood Flow Metab.*, vol. 35, no. 12, pp. 2001–2009, Dec. 2015.

[52] N. M. Alpert, R. D. Badgaiyan, E. Livni, and A. J. Fischman, "A novel method for noninvasive detection of neuromodulatory changes in specific neurotransmitter systems," *Neuroimage*, vol. 19, no. 3, pp. 1049–1060, Jul. 2003.

[53] M. D. Normandin, W. K. Schiffer, and E. D. Morris, "A linear model for estimation of neurotransmitter response profiles from dynamic PET data," *Neuroimage*, vol. 59, no. 3, pp. 2689–2699, Mar. 2012.

[54] E. D. Morris *et al.*, "ntPET: A new application of PET imaging for characterizing the kinetics of endogenous neurotransmitter release," *Mol. Imag.*, vol. 4, no. 4, pp. 473–489, Oct. 2005.

[55] R. E. Carson, "Tracer kinetic modeling," in *Positron Emission Tomography: Basic Science and Clinical Practice*, P. E. Valk, D. L. Bailey, D. W. Townsend, and M. N. Maisey, Eds. London, U.K.: Springer, 2003, pp. 147–179.

[56] R. F. Muzic and B. T. Christian, "Evaluation of objective functions for estimation of kinetic parameters," *Med. Phys.*, vol. 33, no. 2, pp. 342–353, Mar. 2006.

[57] M. Yaqub, R. Boellaard, M. A. Kropholler, and A. A. Lammertsma, "Optimization algorithms and weighting factors for analysis of dynamic PET studies," *Phys. Med. Biol.*, vol. 51, no. 17, pp. 4217–4232, Sep. 2006.

[58] M. Ichise, H. Toyama, R. B. Innis, and R. E. Carson, "Strategies to improve neuroreceptor parameter estimation by linear regression analysis," *J. Cerebr. Blood Flow Metab.*, vol. 22, no. 10, pp. 1271–1281, Oct. 2002.

[59] M. Ichise *et al.*, "Linearized reference tissue parametric imaging methods: Application to [11C]DASB positron emission tomography studies of the serotonin transporter in human brain," *J. Cerebr. Blood Flow Metab.*, vol. 23, no. 9, pp. 1096–1112, Sep. 2003.

[60] R. A. Koeppe, J. E. Holden, and W. R. Ip, "Performance comparison of parameter estimation techniques for the quantitation of local cerebral blood flow by dynamic positron computed tomography," *J. Cerebr. Blood Flow Metab.*, vol. 5, no. 2, pp. 224–234, Jul. 1985.

[61] R. N. Gunn, A. A. Lammertsma, S. P. Hume, and V. J. Cunningham, "Parametric imaging of ligand-receptor binding in PET using a simplified reference region model," *Neuroimage*, vol. 6, no. 4, pp. 279–287, Nov. 1997.

[62] Y. Wu and R. E. Carson, "Noise reduction in the simplified reference tissue model for neuroreceptor functional imaging," *J. Cerebr. Blood Flow Metab.*, vol. 22, no. 12, pp. 1440–1452, Dec. 2002.

[63] R. T. Ogden, "Estimation of kinetic parameters in graphical analysis of PET imaging data," *Stat. Med.*, vol. 22, no. 22, pp. 3557–3568, Nov. 2003.

[64] R. V. Parsey, R. T. Ogden, and J. J. Mann, "Determination of volume of distribution using likelihood estimation in graphical analysis: Elimination of estimation bias," *J. Cerebr. Blood Flow Metab.*, vol. 23, no. 12, pp. 1471–1478, Dec. 2003.

[65] Y. Zhou *et al.*, "A consistent and efficient graphical analysis method to improve the quantification of reversible tracer binding in radioligand receptor dynamic PET studies," *Neuroimage*, vol. 44, no. 3, pp. 661–670, Mar. 2009.

[66] J. van den Hoff, W. Burchert, W. Müller-Schauenburg, G. J. Meyer, and H. Hundeshagen, "Accurate local blood flow measurements with dynamic PET: Fast determination of input function delay and dispersion by multilinear minimization," *J. Nucl. Med.*, vol. 34, no. 10, pp. 1770–1777, Oct. 1993.

[67] D. Feng, Z. Wang, and S.-C. Huang, "A study on statistically reliable and computationally efficient algorithms for generating local cerebral blood flow parametric images with positron emission tomography," *IEEE Trans. Med. Imag.*, vol. 12, no. 2, pp. 182–188, Jun. 1993.

[68] R. Boellaard, P. Knaapen, A. Rijbroek, G. J. J. Luurtsema, and A. A. Lammertsma, "Evaluation of basis function and linear least squares methods for generating parametric blood flow images using 15O-water and positron emission tomography," *Mol. Imag. Biol.*, vol. 7, no. 4, pp. 273–285, Jul. 2005.

[69] Y. Zhou, C. J. Endres, J. R. Brasiæ, S.-C. Huang, and D. F. Wong, "Linear regression with spatial constraint to generate parametric images of ligand-receptor dynamic PET studies with a simplified reference tissue model," *Neuroimage*, vol. 18, no. 4, pp. 975–989, May 2003.

[70] X. Huang, Y. Zhou, S. Bao, and S.-C. Huang, "Clustering-based linear least square fitting method for generation of parametric images in dynamic FDG PET studies," *Int. J. Biomed. Imag.*, vol. 2007, Jul. 2007, Art. no. 65641.

[71] P. Gravel and A. J. Reader, "Direct 4D PET MLEM reconstruction of parametric images using the simplified reference tissue model with the basis function method for [^{11}C]raclopride," *Phys. Med. Biol.*, vol. 60, no. 11, pp. 4533–4549, Jul. 2015.

[72] J. Yan, B. Planeta-Wilson, and R. E. Carson, "Direct 4-D PET list mode parametric reconstruction with a novel EM algorithm," *IEEE Trans. Med. Imag.*, vol. 31, no. 12, pp. 2213–2223, Dec. 2012.

[73] K.-H. Su, T.-C. Yen, and Y.-H. D. Fang, "A novel approach for direct reconstruction of parametric images for myocardial blood flow from PET imaging," *Med. Phys.*, vol. 40, no. 10, Oct. 2013, Art. no. 102505.

[74] G. Wang and J. Qi, "An optimization transfer algorithm for nonlinear parametric image reconstruction from dynamic PET data," *IEEE Trans. Med. Imag.*, vol. 31, no. 10, pp. 1977–1988, Oct. 2012.

[75] M. E. Kamasak, C. A. Bouman, E. D. Morris, and K. Sauer, "Direct reconstruction of kinetic parameter images from dynamic PET data," *IEEE Trans. Med. Imag.*, vol. 24, no. 5, pp. 636–650, May 2005.

[76] L. A. Shepp and Y. Vardi, "Maximum likelihood reconstruction for emission tomography," *IEEE Trans. Med. Imag.*, vol. MI-1, no. 2, pp. 113–122, Oct. 1982.

[77] K. Lange and R. Carson, "EM reconstruction algorithms for emission and transmission tomography," *J. Comput. Assist. Tomo.*, vol. 8, no. 2, pp. 306–316, Apr. 1984.

[78] H. M. Hudson and R. S. Larkin, "Accelerated image reconstruction using ordered subsets of projection data," *IEEE Trans. Med. Imag.*, vol. 13, no. 4, pp. 601–609, Dec. 1994.

[79] J. Tang, H. Kuwabara, D. F. Wong, and A. Rahmim, "Direct 4D reconstruction of parametric images incorporating anato-functional joint entropy," *Phys. Med. Biol.*, vol. 55, no. 15, pp. 4261–4272, Aug. 2010.

[80] J. Matthews, D. Bailey, P. Price, and V. Cunningham, "The direct calculation of parametric images from dynamic PET data using maximum-likelihood iterative reconstruction," *Phys. Med. Biol.*, vol. 42, no. 6, pp. 1155–1173, Jul. 1997.

[81] C. Tsoumpas, F. E. Turkheimer, and K. Thielemans, "Study of direct and indirect parametric estimation methods of linear models in dynamic positron emission tomography," *Med. Phys.*, vol. 35, no. 4, pp. 1299–1309, May 2008.

[82] C. Tsoumpas, F. Turkheimer, and K. Thielemans, "Convergence properties of algorithms for direct parametric estimation of linear models in dynamic PET," in *Proc. IEEE Nucl. Sci. Symp. Med. Imag. Conf.*, Honolulu, HI, USA, 2007, pp. 3034–3037.

[83] A. J. Reader *et al.*, "Fully 4D image reconstruction by estimation of an input function and spectral coefficients," in *Proc. IEEE Nucl. Sci. Symp. Med. Imag. Conf.*, Honolulu, HI, USA, 2007, pp. 3260–3267.

[84] M. Germino, J.-D. Gallezot, J. Yan, and R. E. Carson, "Direct reconstruction of parametric images for brain PET with event-by-event motion correction: Evaluation in two tracers across count levels," *Phys. Med. Biol.*, vol. 62, no. 13, pp. 5344–5364, Jul. 2017.

[85] M. Germino and R. E. Carson, "Cardiac-gated parametric images from ^{82}Rb PET from dynamic frames and direct 4D reconstruction," *Med. Phys.*, vol. 45, no. 2, pp. 639–654, Feb. 2018. doi: 10.1002/mp.12710.

[86] A. Rahmim *et al.*, "Direct 4D parametric imaging for linearized models of reversibly binding PET tracers using generalized AB-EM reconstruction," *Phys. Med. Biol.*, vol. 57, no. 3, pp. 733–755, Mar. 2012.

[87] G. Wang and J. Qi, "Direct estimation of kinetic parametric images for dynamic PET," *Theranostics*, vol. 3, no. 10, pp. 802–815, Nov. 2013.

[88] J.-D. Gallezot, M. K. Germino, and R. E. Carson, "Direct EM reconstruction of parametric images from list-mode brain PET using a novel model based on Logan graphical analysis," in *Proc. IEEE Nucl. Sci. Symp. Med. Imag. Conf.*, Strasbourg, France, 2016, pp. 1–4.

[89] A. J. Reader and J. Verhaeghe, "4D image reconstruction for emission tomography," *Phys. Med. Biol.*, vol. 59, no. 22, pp. R371–R418, Nov. 2014.

[90] G. Wang and J. Qi, "Acceleration of the direct reconstruction of linear parametric images using nested algorithms," *Phys. Med. Biol.*, vol. 55, no. 5, pp. 1505–1517, Apr. 2010.

[91] T. Merlin, P. Fernandez, D. Visvikis, and F. Lamare, "Direct 4D Patlak parametric image reconstruction algorithm integrating respiratory motion correction for oncology studies," in *Proc. IEEE Nucl. Sci. Symp. Med. Imag. Conf.*, Seoul, South Korea, 2013, pp. 1–6.

[92] R. E. Carson, W. C. Barker, J.-S. Liow, and C. A. Johnson, "Design of a motion-compensation OSEM list-mode algorithm for resolution-recovery reconstruction for the HRRT," in *Proc. IEEE Nucl. Sci. Symp. Conf. Rec.*, vol. 5. Portland, OR, USA, 2003, pp. 3281–3285.

[93] J. Q. Jiao *et al.*, "Direct parametric reconstruction with joint motion estimation/correction for dynamic brain PET data," *IEEE Trans. Med. Imag.*, vol. 36, no. 1, pp. 203–213, Jan. 2017.

[94] F. A. Kotasidis *et al.*, "Impact of erroneous kinetic model formulation in direct 4D image reconstruction," in *Proc. IEEE Nucl. Sci. Symp. Med. Imag. Conf.*, Valencia, Spain, 2011, pp. 2366–2367.

[95] F. A. Kotasidis, J. C. Matthews, A. J. Reader, G. I. Angelis, and H. Zaidi, "Application of adaptive kinetic modelling for bias propagation reduction in direct 4D image reconstruction," *Phys. Med. Biol.*, vol. 59, no. 20, pp. 6061–6084, Oct. 2014.

[96] J. C. Matthews *et al.*, "Adaptive parametric kinetic modelling for improved full field of view fitting of PET data," in *Proc. IEEE Nucl. Sci. Symp. Med. Imag. Conf.*, Anaheim, CA, USA, 2012, pp. 3925–3929.

[97] R. Loeb, N. Navab, and S. I. Ziegler, "Direct parametric reconstruction using anatomical regularization for simultaneous PET/MRI data," *IEEE Trans. Med. Imag.*, vol. 34, no. 11, pp. 2233–2247, Nov. 2015.

[98] K. Gong *et al.*, "Direct Patlak reconstruction from dynamic PET data using the kernel method with MRI information based on structural similarity," *IEEE Trans. Med. Imag.*, vol. 37, no. 4, pp. 955–965, Apr. 2018.

[99] M. Tonietto *et al.*, "Plasma radiometabolite correction in dynamic PET studies: Insights on the available modeling approaches," *J. Cerebr. Blood Flow Metab.*, vol. 36, no. 2, pp. 326–339, Feb. 2016.

[100] F. E. Froklage *et al.*, "Quantification of 11C-laniquidar kinetics in the brain," *J. Nucl. Med.*, vol. 56, no. 11, pp. 1730–1735, Nov. 2015.

[101] M. Fujita *et al.*, "Kinetic and equilibrium analyses of [(123)I]epidepride binding to striatal and extrastriatal dopamine D(2) receptors," *Synapse*, vol. 34, no. 4, pp. 290–304, Dec. 1999.

[102] Y. Kimura *et al.*, "PET quantification of tau pathology in human brain with 11C-PBB3," *J. Nucl. Med.*, vol. 56, no. 9, pp. 1359–1365, Sep. 2015.

[103] K. Takahata *et al.*, "A human PET study of [11C]HMS011, a potential radioligand for AMPA receptors," *EJNMMI Res.*, vol. 7, no. 1, p. 63, Aug. 2017.

[104] A. Varrone *et al.*, "Kinetic analysis and quantification of the dopamine transporter in the nonhuman primate brain with 11C-PE2I and 18F-FE-PE2I," *J. Nucl. Med.*, vol. 52, no. 1, pp. 132–139, Feb. 2011.

[105] J. C. Price *et al.*, "Analyses of [(18)F] altanserin bolus injection PET data. I: Consideration of radiolabeled metabolites in baboons," *Synapse*, vol. 41, no. 1, pp. 1–10, Jul. 2001.

[106] J. C. Price *et al.*, "Analyses of [(18)F]altanserin bolus injection PET data. II: Consideration of radiolabeled metabolites in humans," *Synapse*, vol. 41, no. 1, pp. 11–21, Jul. 2001.

[107] A. A. Lammertsma *et al.*, "The C15O2 build-up technique to measure regional cerebral blood flow and volume of distribution of water," *J. Cerebr. Blood Flow Metab.*, vol. 9, no. 4, pp. 461–470, Aug. 1989.

[108] E. Meyer, "Simultaneous correction for tracer arrival delay and dispersion in CBF measurements by the H215O autoradiographic method and dynamic PET," *J. Nucl. Med.*, vol. 30, no. 6, pp. 1069–1078, Jul. 1989.

[109] A. A. Lammertsma, *Quantification of Cerebral Blood Flow*. Totowa, NJ, USA: Humana Press, 2012, ch. 43, pp. 99–109.

[110] I. Kanno *et al.*, "Measurement of cerebral blood flow using bolus inhalation of C15O2 and positron emission tomography: Description of the method and its comparison with the C15O2 continuous inhalation method," *J. Cerebr. Blood Flow Metab.*, vol. 4, no. 2, pp. 224–234, Jul. 1984.

[111] R. Boellaard, A. van Lingen, S. C. van Balen, B. G. Hoving, and A. A. Lammertsma, "Characteristics of a new fully programmable blood sampling device for monitoring blood radioactivity during PET," *Eur. J. Nucl. Med.*, vol. 28, no. 1, pp. 81–89, Feb. 2001.

[112] J. O'Doherty, A. Chilcott, and J. Dunn, "Effect of tubing length on the dispersion correction of an arterially sampled input function for kinetic modeling in PET," *Nucl. Med. Commun.*, vol. 36, no. 11, pp. 1143–1149, Nov. 2015.

[113] M.-C. Asselin, L. M. Wahl, V. J. Cunningham, S. Amano, and C. Nahmias, "In vivo metabolism and partitioning of 6-[18F]fluoro-L-meta-tyrosine in whole blood: A unified compartment model," *Phys. Med. Biol.*, vol. 47, no. 11, pp. 1961–1977, Jul. 2002.

[114] C. Nahmias, L. M. Wahl, S. Amano, M.-C. Asselin, and R. Chirakal, "Equilibration of 6-[18F]fluoro-L-m-tyrosine between plasma and erythrocytes," *J. Nucl. Med.*, vol. 41, no. 10, pp. 1636–1641, Oct. 2000.

[115] B. Foster, U. Bagci, A. Mansoor, Z. Xu, and D. J. Mollura, "A review on segmentation of positron emission tomography images," *Comput. Biol. Med.*, vol. 50, pp. 76–96, Jul. 2014.

[116] Y. Tao, Z. Peng, A. Krishnan, and X. S. Zhou, "Robust learning-based parsing and annotation of medical radiographs," *IEEE Trans. Med. Imag.*, vol. 30, no. 2, pp. 338–350, Feb. 2011.

[117] O. C. Avila-Montes *et al.*, "Segmentation of the thoracic aorta in non-contrast cardiac CT images," *IEEE J. Biomed. Health Inform.*, vol. 17, no. 5, pp. 936–949, Sep. 2013.

[118] Y. Zhu, X. Papademetris, A. J. Sinusas, and J. S. Duncan, "Segmentation of the left ventricle from cardiac MR images using a subject-specific dynamical model," *IEEE Trans. Med. Imag.*, vol. 29, no. 3, pp. 669–687, Mar. 2010.

[119] Y. Xie, J. Padgett, A. M. Biancardi, and A. P. Reeves, "Automated aorta segmentation in low-dose chest CT images," *Int. J. Comput. Assist. Radiol. Surg.*, vol. 9, no. 2, pp. 211–219, Mar. 2014.

[120] J. Krejza *et al.*, "Carotid artery diameter in men and women and the relation to body and neck size," *Stroke*, vol. 37, no. 4, pp. 1103–1105, Apr. 2006.

[121] J. G. Terry *et al.*, "Carotid arterial structure in patients with documented coronary artery disease and disease-free control subjects," *Circulation*, vol. 107, no. 8, pp. 1146–1151, Mar. 2003.

[122] P. Zanotti-Fregonara *et al.*, "Comparison of eight methods for the estimation of the image-derived input function in dynamic [(18)F]-FDG PET human brain studies," *J. Cerebr. Blood Flow Metab.*, vol. 29, no. 11, pp. 1825–1835, Nov. 2009.

[123] K. Chen *et al.*, "Noninvasive quantification of the cerebral metabolic rate for glucose using positron emission tomography, 18F-fluoro-2-deoxyglucose, the Patlak method, and an image-derived input function," *J. Cerebr. Blood Flow Metab.*, vol. 18, no. 7, pp. 716–723, Jul. 1998.

[124] P. Zanotti-Fregonara, K. Chen, J. S. Liow, M. Fujita, and R. B. Innis, "Image-derived input function for brain PET studies: Many challenges and few opportunities," *J. Cerebr. Blood Flow Metab.*, vol. 31, no. 10, pp. 1986–1998, Oct. 2011.

[125] Y. Choi *et al.*, "Parametric images of myocardial metabolic rate of glucose generated from dynamic cardiac PET and 2-[18F]fluoro-2-deoxy-d-glucose studies," *J. Nucl. Med.*, vol. 32, no. 4, pp. 733–738, Apr. 1991.

[126] L. F. de Geus-Oei *et al.*, "Comparison of image-derived and arterial input functions for estimating the rate of glucose metabolism in therapy-monitoring 18F-FDG PET studies," *J. Nucl. Med.*, vol. 47, no. 6, pp. 945–949, Jun. 2006.

[127] C. J. Hoekstra, O. S. Hoekstra, and A. A. Lammertsma, "On the use of image-derived input functions in oncological fluorine-18 fluorodeoxyglucose positron emission tomography studies," *Eur. J. Nucl. Med.*, vol. 26, no. 11, pp. 1489–1492, Nov. 1999.

[128] A. P. van der Weerdt *et al.*, "Image-derived input functions for determination of MRGlu in cardiac (18)F-FDG PET scans," *J. Nucl. Med.*, vol. 42, no. 11, pp. 1622–1629, Nov. 2001.

[129] W. Watabe *et al.*, "Noninvasive estimation of the aorta input function for measurement of tumor blood flow with [15/O]water]," *IEEE Trans. Med. Imag.*, vol. 20, no. 3, pp. 164–174, Mar. 2001.

[130] P. Zanotti-Fregonara *et al.*, "Image-derived input function in PET brain studies: Blood-based methods are resistant to motion artifacts," *Nucl. Med. Commun.*, vol. 33, no. 9, pp. 982–989, Sep. 2012.

[131] S. Takikawa *et al.*, "Noninvasive quantitative fluorodeoxyglucose PET studies with an estimated input function derived from a population-based arterial blood curve," *Radiology*, vol. 188, no. 1, pp. 131–136, Jul. 1993.

[132] T. Tsuchida *et al.*, "Noninvasive measurement of cerebral metabolic rate of glucose using standardized input function," *J. Nucl. Med.*, vol. 40, no. 9, pp. 1441–1445, Sep. 1999.

[133] T. Shiozaki *et al.*, "Noninvasive estimation of FDG input function for quantification of cerebral metabolic rate of glucose: Optimization and multicenter evaluation," *J. Nucl. Med.*, vol. 41, no. 10, pp. 1612–1618, Oct. 2000.

[134] S. Eberl, A. R. Anayat, R. R. Fulton, P. K. Hooper, and M. J. Fulham, "Evaluation of two population-based input functions for quantitative neurological FDG PET studies," *Eur. J. Nucl. Med.*, vol. 24, no. 3, pp. 299–304, Mar. 1997.

[135] D. Vriens, L. F. de Geus-Oei, W. J. Oyen, and E. P. Visser, "A curve-fitting approach to estimate the arterial plasma input function for the assessment of glucose metabolic rate and response to treatment," *J. Nucl. Med.*, vol. 50, no. 12, pp. 1933–1939, Dec. 2009.

[136] M. Bentourkia, "Kinetic modeling of PET-FDG in the brain without blood sampling," *Comput. Med. Imag. Graph.*, vol. 30, no. 8, pp. 447–451, Dec. 2006.

[137] Y. Huang *et al.*, "A new positron emission tomography imaging agent for the serotonin transporter: Synthesis, pharmacological characterization, and kinetic analysis of [11C]2-[2-(dimethylaminomethyl)phenylthio]-5-fluoromethylphenylamine ([11C]AFM)," *Nucl. Med. Biol.*, vol. 31, no. 5, pp. 543–556, Jul. 2004.

[138] S. S. Gambhir *et al.*, "Simple noninvasive quantification method for measuring myocardial glucose utilization in humans employing positron emission tomography and fluorine-18 deoxyglucose," *J. Nucl. Med.*, vol. 30, no. 3, pp. 359–366, Apr. 1989.

[139] R. T. Ogden, F. Zanderigo, S. Choy, J. J. Mann, and R. V. Parsey, "Simultaneous estimation of input functions: An empirical study," *J. Cereb. Blood Flow Metab.*, vol. 30, no. 4, pp. 816–826, Apr. 2010.

[140] Z. Bian *et al.*, "Dynamic positron emission tomography image restoration via a kinetics-induced bilateral filter," *PLoS ONE*, vol. 9, no. 2, 2014, Art. no. e89282.

[141] D. N. Greve *et al.*, "Cortical surface-based analysis reduces bias and variance in kinetic modeling of brain PET data," *Neuroimage*, vol. 92, pp. 225–236, Jun. 2014.

[142] F. E. Turkheimer, M. Brett, D. Visvikis, and V. J. Cunningham, "Multiresolution analysis of emission tomography images in the wavelet domain," *J. Cereb. Blood Flow Metab.*, vol. 19, no. 11, pp. 1189–1208, Nov. 1999.

[143] Z. Cselényi, H. Olsson, C. Halldin, B. Gulyás, and L. Farde, "A comparison of recent parametric neuroreceptor mapping approaches based on measurements with the high affinity PET radioligands [11C]FLB 457 and [11C]WAY 100635," *Neuroimage*, vol. 32, no. 4, pp. 1690–1708, Oct. 2006.

[144] F. E. Turkheimer, J. A. D. Aston, R. B. Banati, C. Riddell, and V. J. Cunningham, "A linear wavelet filter for parametric imaging with dynamic PET," *IEEE Trans. Med. Imag.*, vol. 22, no. 3, pp. 289–301, Mar. 2003.

[145] F. E. Turkheimer *et al.*, "Modeling dynamic PET-SPECT studies in the wavelet domain," *J. Cereb. Blood Flow Metab.*, vol. 20, no. 5, pp. 879–893, Jun. 2000.

[146] N. M. Alpert, A. Reilhac, T. C. Chio, and I. Selesnick, "Optimization of dynamic measurement of receptor kinetics by wavelet denoising," *Neuroimage*, vol. 30, no. 2, pp. 444–451, May 2006.

[147] J.-D. Gallezot *et al.*, "Parametric imaging and test-retest variability of 11C-(+)-PHNO binding to D_2/D_3 dopamine receptors in humans on the high-resolution research tomograph PET scanner," *J. Nucl. Med.*, vol. 55, no. 6, pp. 960–966, May 2014.

[148] M. Yaqub, R. Boellaard, A. Schuitemaker, B. N. M. van Berckel, and A. A. Lammertsmae, "Impact of wavelet based denoising of [11C](R)-PK11195 time activity curves on accuracy and precision of kinetic analysis," *Med. Phys.*, vol. 35, no. 11, pp. 5069–5078, Nov. 2008.

[149] P. Millet *et al.*, "Quantification of dopamine D(2/3) receptors in rat brain using factor analysis corrected [18F]Fallypride images," *Neuroimage*, vol. 62, no. 3, pp. 1455–1468, Sep. 2012. doi: 10.1016/j.neuroimage.2012.05.075.

[150] C.-R. Jiang, J. A. D. Aston, and J.-L. Wang, "Smoothing dynamic positron emission tomography time courses using functional principal components," *Neuroimage*, vol. 47, no. 1, pp. 184–193, Aug. 2009.

[151] A. D. Joshi, J. A. Fessler, and R. A. Koeppe, "Improving PET receptor binding estimates from Logan plots using principal component analysis," *J. Cereb. Blood Flow Metab.*, vol. 28, no. 4, pp. 852–865, May 2008.

[152] G. El Fakhri *et al.*, "Quantitative dynamic cardiac 82Rb PET using generalized factor and compartment analyses," *J. Nucl. Med.*, vol. 46, no. 8, pp. 1264–1271, Aug. 2005.

[153] Y. Kimura, M. Senda, and N. M. Alpert, "Fast formation of statistically reliable FDG parametric images based on clustering and principal components," *Phys. Med. Biol.*, vol. 47, no. 3, pp. 455–468, Mar. 2002.

[154] O. Tichy and V. Smidl, "Bayesian blind separation and deconvolution of dynamic image sequences using sparsity priors," *IEEE Trans. Med. Imag.*, vol. 34, no. 1, pp. 258–266, Feb. 2015.

[155] Y. Su, M. J. Welch, and K. I. Shoghi, "The application of maximum likelihood factor analysis (MLFA) with uniqueness constraints on dynamic cardiac microPET data," *Phys. Med. Biol.*, vol. 52, no. 8, pp. 2313–2334, May 2007.

[156] K. M. Johnson *et al.*, "Improved waveform fidelity using local HYPR reconstruction (HYPR LR)," *Magn. Reson. Med.*, vol. 59, no. 3, pp. 456–462, Apr. 2008.

[157] B. T. Christian, N. T. Vandehey, J. M. Floberg, and C. A. Mistretta, "Dynamic PET denoising with HYPR processing," *J. Nucl. Med.*, vol. 51, no. 7, pp. 1147–1154, Jul. 2010.

[158] J. M. Floberg *et al.*, "Improved kinetic analysis of dynamic PET data with optimized HYPR-LR," *Med. Phys.*, vol. 39, no. 6, pp. 3319–3331, Jul. 2012.

[159] B. Spencer, J. Qi, R. D. Badawi, and G. Wang, "Dynamic PET image reconstruction for parametric imaging using the HYPR kernel method," in *Proc. SPIE Med. Imag.*, 2017, Art. no. 101324W.

[160] K. He, J. Sun, and X. Tang, "Guided image filtering," *IEEE Trans. Pattern Anal. Mach. Intell.*, vol. 35, no. 6, pp. 1397–1409, Jul. 2013.

[161] K. He, J. Sun, and X. Tang, "Guided image filtering," in *Computer Vision—ECCV 2010* (LNCS 6311), K. Daniilidis, P. Maragos, and N. Paragios, Eds. Heidelberg, Germany: Springer, 2010, pp. 1–14.

[162] F. Hashimoto, H. Ohba, K. Ote, and H. Tsukada, "Denoising of dynamic sinogram by image guided filtering for positron emission tomography," *IEEE Trans. Radiat. Plasma Med. Sci.*, vol. 2, no. 6, pp. 541–548, Nov. 2018.

[163] M. Byrtek, F. O'Sullivan, M. Muzi, and A. M. Spence, "An adaptation of ridge regression for improved estimation of kinetic model parameters from PET studies," *IEEE Trans. Nucl. Sci.*, vol. 52, no. 1, pp. 63–68, Feb. 2005.

[164] F. O'Sullivan and A. Saha, "Use of ridge regression for improved estimation of kinetic constants from PET data," *IEEE Trans. Med. Imag.*, vol. 18, no. 2, pp. 115–125, Feb. 1999.

[165] N. M. Alpert and F. Yuan, "A general method of Bayesian estimation for parametric imaging of the brain," *Neuroimage*, vol. 45, no. 4, pp. 1183–1189, Jun. 2009.

[166] Y.-H. D. Fang, G. E. Fakhri, J. A. Becker, and N. M. Alpert, "Parametric imaging with Bayesian priors: A validation study with (11)C-Altropane PET," *Neuroimage*, vol. 61, no. 1, pp. 131–138, Jun. 2012.

[167] A. Bertoldo, G. Sparacino, and C. Cobelli, "'Population' approach improves parameter estimation of kinetic models from dynamic PET data," *IEEE Trans. Med. Imag.*, vol. 23, no. 3, pp. 297–306, Mar. 2004.

[168] G. Tomasi *et al.*, "Global-two-stage filtering of clinical PET parametric maps: Application to [(11)C]-(R)-PK11195," *Neuroimage*, vol. 55, no. 3, pp. 942–953, May 2011.

[169] Y. Zhou, S.-C. Huang, and M. Bergsneider, "Linear ridge regression with spatial constraint for generation of parametric images in dynamic positron emission tomography studies," *IEEE Trans. Nucl. Sci.*, vol. 48, no. 1, pp. 125–130, Feb. 2001.

[170] G. Rizzo *et al.*, "Multi-scale hierarchical generation of PET parametric maps: Application and testing on a [11C]DPN study," *Neuroimage*, vol. 59, no. 3, pp. 2485–2493, Mar. 2012.

[171] Y. Zhou, S.-C. Huang, M. Bergsneider, and D. F. Wong, "Improved parametric image generation using spatial–temporal analysis of dynamic PET studies," *Neuroimage*, vol. 15, no. 3, pp. 697–707, Apr. 2002.

[172] J. B. Mandeville *et al.*, "A regularized full reference tissue model for PET neuroreceptor mapping," *Neuroimage*, vol. 139, pp. 405–414, Oct. 2016.

[173] M. M. Ter-Pogossian, S. R. Bergmann, and B. E. Sobel, "Influence of cardiac and respiratory motion on tomographic reconstructions of the heart: Implications for quantitative nuclear cardiology," *J. Comput. Assisted Tomography*, vol. 6, no. 6, pp. 1148–1155, 1982.

[174] M. Bergström *et al.*, "Head fixation device for reproducible position alignment in transmission CT and positron emission tomography," *J. Comput. Assisted Tomography*, vol. 5, no. 1, pp. 136–141, 1981.

[175] M. V. Green *et al.*, "Head movement in normal subjects during simulated PET brain imaging with and without head restraint," *J. Nucl. Med.*, vol. 35, no. 9, pp. 1538–1546, 1994.

[176] U. E. Ruttimann, P. J. Andreason, and D. Rio, "Head motion during positron emission tomography: Is it significant?" *Psychiatry Res.*, vol. 61, no. 1, pp. 43–51, 1995.

[177] O. Parodi *et al.*, "Cardiac emission computed tomography: Underestimation of regional tracer concentrations due to wall motion abnormalities," *J. Comput. Assisted Tomography*, vol. 8, no. 6, pp. 1083–1092, 1984.

[178] Y. Nakamoto *et al.*, "PET/CT: Artifacts caused by bowel motion," *Nucl. Med. Commun.*, vol. 25, no. 3, pp. 221–225, Mar. 2004.

[179] Y. Lu *et al.*, "Respiratory motion compensation for PET/CT with motion information derived from matched attenuation-corrected gated PET data," *J. Nucl. Med.*, vol. 59, no. 9, pp. 1480–1486, 2018.

[180] W. G. O'Dell, C. C. Moore, W. C. Hunter, E. A. Zerhouni, and E. R. Mcveigh, "Three-dimensional myocardial deformations: Calculation with displacement field fitting to tagged MR images," *Radiology* vol. 195, no. 3, pp. 829–835, 1995.

[181] J. M. Mukherjee, K. L. Johnson, J. E. Mcnamara, and M. A. King, "Quantitative study of rigid-body and respiratory motion of patients undergoing stress and rest cardiac SPECT imaging," *IEEE Trans. Nucl. Sci.*, vol. 57, no. 3, pp. 1105–1115, Jun. 2010.

[182] G. W. Goerres *et al.*, "Respiration-induced attenuation artifact at PET/CT: Technical considerations," *Radiology*, vol. 226, no. 3, pp. 906–910, Mar. 2003.

[183] C. R. Hunter, R. Klein, R. S. Beanlands, and R. A. Dekemp, "Patient motion effects on the quantification of regional myocardial blood flow with dynamic PET imaging," *Med. Phys.*, vol. 43, no. 4, pp. 1829–1840, Apr. 2016.

[184] Y. H. Yu *et al.*, "Event-by-event continuous respiratory motion correction for dynamic PET imaging," *J. Nucl. Med.*, vol. 57, no. 7, pp. 1084–1090, Jul. 2016.

[185] F. A. Kotasidis *et al.*, "Impact of motion on indirect and direct reconstruction of kinetic parameters from dynamic PET data," in *Proc. IEEE Nucl. Sci. Symp. Med. Imag. Conf. Rec.*, 2013, pp. 1–4.

[186] P. J. Keall *et al.*, "The management of respiratory motion in radiation oncology report of AAPM task group 76," *Med. Phys.*, vol. 33, no. 10, pp. 3874–3900, Oct. 2006.

[187] J. F. He *et al.*, "A novel method for respiratory motion gated with geometric sensitivity of the scanner in 3D PET," *IEEE Trans. Nucl. Sci.*, vol. 55, no. 5, pp. 2557–2565, Oct. 2008.

[188] P. J. Schleyer, M. J. O'Doherty, S. F. Barrington, and P. K. Marsden, "Retrospective data-driven respiratory gating for PET/CT," *Phys. Med. Biol.*, vol. 54, no. 7, pp. 1935–1950, 2009.

[189] A. L. Kesner and C. Kuntner, "A new fast and fully automated software based algorithm for extracting respiratory signal from raw PET data and its comparison to other methods," *Med. Phys.*, vol. 37, no. 10, pp. 5550–5559, Oct. 2010.

[190] F. Buther *et al.*, "Detection of respiratory tumour motion using intrinsic list mode-driven gating in positron emission tomography," *Eur. J. Nucl. Med. Mol. Imag.*, vol. 37, no. 12, pp. 2315–2327, 2010.

[191] P. J. Schleyer, M. J. O'Doherty, and P. K. Marsden, "Extension of a data-driven gating technique to 3D, whole body PET studies," *Phys. Med. Biol.*, vol. 56, no. 13, pp. 3953–3965, 2011.

[192] A. L. Kesner *et al.*, "On transcending the impasse of respiratory motion correction applications in routine clinical imaging—A consideration of a fully automated data driven motion control framework," *EJNMMI Phys.*, vol. 1, no. 1, p. 8, Dec. 2014.

[193] S. Ren *et al.*, "Data-driven event-by-event respiratory motion correction using TOF PET list-mode centroid of distribution," *Phys. Med. Biol.*, vol. 62, no. 12, pp. 4741–4755, 2017.

[194] A. L. Kesner, J. G. Meier, D. D. Burckhardt, J. Schwartz, and D. A. Lynch, "Data-driven optimal binning for respiratory motion management in PET," *Med. Phys.*, vol. 45, no. 1, pp. 277–286, 2018.

[195] O. Bertolli *et al.*, "Sign determination methods for the respiratory signal in data-driven PET gating," *Phys. Med. Biol.*, vol. 62, no. 8, pp. 3204–3220, Apr. 2017.

[196] S. A. Nehmeh *et al.*, "Effect of respiratory gating on quantifying PET images of lung cancer," *J. Nucl. Med.*, vol. 43, no. 7, pp. 876–881, Jul. 2002.

[197] C. Liu *et al.*, "Quiescent period respiratory gating for PET/CT," *Med. Phys.*, vol. 37, no. 9, pp. 5037–5043, Sep. 2010.

[198] A. L. Kesner *et al.*, "Validation of software gating: A practical technology for respiratory motion correction in PET," *Radiology*, vol. 281, no. 1, pp. 239–248, Oct. 2016. doi: 10.1148/radiol.2016152105.

[199] W. van Elmpt *et al.*, "Optimal gating compared to 3D and 4D PET reconstruction for characterization of lung tumours," *Eur. J. Nucl. Med. Mol. Imag.*, vol. 38, no. 5, pp. 843–855, May 2011.

[200] S. A. Nehmeh and Y. E. Erdi, "Respiratory motion in positron emission tomography/computed tomography: A review," *Seminars Nucl. Med.*, vol. 38, no. 3, pp. 167–176, 2008.

[201] F. Lamare *et al.*, "Respiratory motion correction for PET oncology applications using affine transformation of list mode data," *Phys. Med. Biol.*, vol. 52, no. 1, pp. 121–140, 2006.

[202] M. Dawood, N. Lang, X. Jiang, and K. P. Schafers, "Lung motion correction on respiratory gated 3-D PET/CT images," *IEEE Trans. Med. Imag.*, vol. 25, no. 4, pp. 476–485, Apr. 2006.

[203] A. Rahmim, J. Tang, M. R. Ay, and F. M. Bengel, "4D respiratory motion-corrected Rb-82 myocardial perfusion PET image reconstruction," in *Proc. IEEE Nucl. Sci. Symp. Med. Imag. Conf.*, 2010, pp. 3312–3316.

[204] I. Polycarpou, C. Tsoumpas, and P. K. Marsden, "Analysis and comparison of two methods for motion correction in PET imaging," *Med. Phys.*, vol. 39, no. 10, pp. 6474–6483, 2012. doi: 10.1118/1.4754586.

[205] F. Qiao, T. Pan, J. W. Clark, and O. R. Mawlawi, "A motion-incorporated reconstruction method for gated PET studies," *Phys. Med. Biol.*, vol. 51, no. 15, pp. 3769–3783, 2006.

[206] J. Qi and R. H. Huesman, "List mode reconstruction for pet with motion compensation: A simulation study," in *Proc. IEEE Int. Symp. Biomed. Imag.*, Washington, DC, USA, 2002, pp. 413–416.

[207] T. Li, B. Thorndyke, E. Schreibmann, Y. Yang, and L. Xing, "Model-based image reconstruction for four dimensional PET," *Med. Phys.*, vol. 33, no. 5, pp. 1288–1298, 2006.

[208] R. Manjeshwar, X. D. Tao, E. Asma, and K. Thielemans, "Motion compensated image reconstruction of respiratory gated PET/CT," in *Proc. 3rd IEEE Int. Symp. Biomed. Imag. Macro Nano*, vol. 1, no. 3, 2006, pp. 674–677.

[209] D. Visvikis, F. Lamare, P. Bruyant, N. Boussion, and C. C. Le Rest, "Respiratory motion in positron emission tomography for oncology applications: Problems and solutions," *Nucl. Instrum. Methods Phys. Res. A Accelerators Spectrometers Detectors Assoc. Equip.*, vol. 569, no. 2, pp. 453–457, 2006.

[210] W. Bai and M. Brady, "Motion correction and attenuation correction for respiratory gated PET images," *IEEE Trans. Med. Imag.*, vol. 30, no. 2, pp. 351–365, Feb. 2011.

[211] F. Lamare *et al.*, "List-mode-based reconstruction for respiratory motion correction in PET using non-rigid body transformations," *Phys. Med. Biol.*, vol. 52, no. 17, pp. 5187–5204, Sep. 2007.

[212] M. Reyes, G. Malandain, P. M. Koulibaly, M. A. González-Ballester, and J. Darcourt, "Model-based respiratory motion compensation for emission tomography image reconstruction," *Phys. Med. Biol.*, vol. 52, no. 12, pp. 3579–3600, 2007.

[213] M. Dawood, F. Buther, X. Y. Jiang, and K. P. Schafers, "Respiratory motion correction in 3-D PET data with advanced optical flow algorithms," *IEEE Trans. Med. Imag.*, vol. 27, no. 8, pp. 1164–1175, Aug. 2008.

[214] W. Bai and M. Brady, "Regularized B-spline deformable registration for respiratory motion correction in PET images," *Phys. Med. Biol.*, vol. 54, no. 9, pp. 2719–2736, 2019. doi: 10.1088/0031-9155/54/9/008.

[215] L. Fin, P. Bailly, J. Daouk, and M. E. Meyer, "Motion correction based on an appropriate system matrix for statistical reconstruction of respiratory-correlated PET acquisitions," *Comput. Methods Programs Biomed.*, vol. 96, no. 3, pp. 1–9. 2009.

[216] F. Gigengack *et al.*, "Motion correction in dual gated cardiac PET using mass-preserving image registration," *IEEE Trans. Med. Imag.*, vol. 31, no. 3, pp. 698–712, Mar. 2012.

[217] M. Fieseler *et al.*, "A dynamic thorax phantom for the assessment of cardiac and respiratory motion correction in PET/MRI: A preliminary evaluation," *Nucl. Instrum. Methods Phys. Res. A Accelerators Spectrometers Detectors Assoc. Equip.*, vol. 702, pp. 59–63, Feb. 2013.

[218] Y. Lu *et al.*, "Investigation of sub-centimeter lung nodule quantification for low-dose PET," *IEEE Trans. Radiat. Plasma Med. Sci.*, vol. 2, no. 1, pp. 1–10, Jan. 2018.

[219] G. J. Klein, B. W. Reutter, and R. H. Huesman, "Non-rigid summing of gated PET via optical flow," *IEEE Trans. Nucl. Sci.*, vol. 44, no. 4, pp. 1509–1512, Aug. 1997.

[220] C. Liu, L. A. Pierce, A. M. Alessio, and P. E. Kinahan, "The impact of respiratory motion on tumor quantification and delineation in static PET/CT imaging," *Phys. Med. Biol.*, vol. 54, no. 24, pp. 7345–7362, Dec. 2009.

[221] C. Chan *et al.*, "Non-rigid event-by-event continuous respiratory motion compensated list-mode reconstruction for PET," *IEEE Trans. Med. Imag.*, vol. 37, no. 2, pp. 504–515, Feb. 2018.

[222] C. Chan *et al.*, "Event-by-event respiratory motion correction for PET with 3D internal-1D external motion correlation," *Med. Phys.*, vol. 40, no. 11, 2013, Art. no. 112507.

[223] G. Bonanno *et al.*, "Self-navigation with compressed sensing for 2D translational motion correction in free-breathing coronary MRI: A feasibility study," *PLoS ONE*, vol. 9, no. 8, 2014, Art. no. e105523.

[224] A. P. King, C. Buerger, C. Tsoumpas, P. K. Marsden, and T. Schaeffter, "Thoracic respiratory motion estimation from MRI using a statistical model and a 2-D image navigator," *Med. Image Anal.*, vol. 16, no. 1, pp. 252–264, Feb. 2012.

[225] S. Y. Chun *et al.*, "MRI-based nonrigid motion correction in simultaneous PET/MRI," *J. Nucl. Med.*, vol. 53, no. 8, pp. 1284–1291, Aug. 2012.

[226] L. Axel and L. Dougherty, "MR imaging of motion with spatial modulation of magnetization," *Radiology*, vol. 171, no. 3, pp. 841–845, Jul. 1989.

[227] J. L. Prince and E. R. McVeigh, "Motion estimation from tagged MR image sequences," *IEEE Trans. Med. Imag.*, vol. 11, no. 2, pp. 238–249, Jun. 1992.

[228] C. Kolbitsch *et al.*, "Cardiac and respiratory motion correction for simultaneous cardiac PET/MR," *J. Nucl. Med.*, vol. 58, no. 5, pp. 846–852, Jun. 2017.

[229] J. Cabello and S. I. Ziegler, "Advances in PET/MR instrumentation and image reconstruction," *Brit. J. Radiol.*, vol. 91, no. 1081, Feb. 2018, Art. no. 20160363.

[230] A. Gillman, J. Smith, P. Thomas, S. Rose, and N. Dowson, "PET motion correction in context of integrated PET/MR: Current techniques, limitations, and future projections," *Med. Phys.*, vol. 44, no. 12, pp. e430–e445, Dec. 2017.

[231] C. Catana, "Motion correction options in PET/MRI," *Seminars Nucl. Med.*, vol. 45, no. 3, pp. 212–223, Jun. 2015.

[232] T. Beyer, L. Tellmann, I. Nickel, and U. Pietrzyk, "On the use of positioning aids to reduce misregistration in the head and neck in whole-body PET/CT studies," *J. Nucl. Med.*, vol. 46, no. 4, pp. 596–602, Apr. 2005.

[233] M. Menke, M. S. Atkins, and K. R. Buckley, "Compensation methods for head motion detected during PET imaging," *IEEE Trans. Nucl. Sci.*, vol. 43, no. 1, pp. 310–317, Feb. 1996.

[234] Y. Picard and C. J. Thompson, "Motion correction of PET images using multiple acquisition frames," *IEEE Trans. Med. Imag.*, vol. 16, no. 2, pp. 137–144, Apr. 1997.

[235] S. R. Goldstein, M. E. Daube-Witherspoon, M. V. Green, and A. Eidsath, "A head motion measurement system suitable for emission computed tomography," *IEEE Trans. Med. Imag.*, vol. 16, no. 1, pp. 17–27, Feb. 1997.

[236] R. R. Fulton *et al.*, "Correction for head movements in positron emission tomography using an optical motion-tracking system," *IEEE Trans. Nucl. Sci.*, vol. 49, no. 1, pp. 116–123, Feb. 2002.

[237] P. M. Bloomfield *et al.*, "The design and implementation of a motion correction scheme for neurological PET," *Phys. Med. Biol.*, vol. 48, no. 8, pp. 959–978, Apr. 2003.

[238] P. Buhler, U. Just, E. Will, J. Kotzerke, and J. Hoff, "An accurate method for correction of head movement in PET," *IEEE Trans. Med. Imag.*, vol. 23, no. 9, pp. 1176–1185, Sep. 2004.

[239] R. Fulton *et al.*, "Accuracy of motion correction methods for PET brain imaging," in *Proc. IEEE Nucl. Sci. Symp. Conf. Rec.*, vol. 7, 2004, pp. 4226–4230.

[240] H. Herzog *et al.*, "Motion artifact reduction on parametric PET images of neuroreceptor binding," *J. Nucl. Med.*, vol. 46, no. 6, pp. 1059–1065, 2005.

[241] A. J. Montgomery *et al.*, "Correction of head movement on PET studies: Comparison of methods," *J. Nucl. Med.*, vol. 47, no. 12, pp. 1936–1944, 2006.

[242] S. H. Keller *et al.*, "Methods for motion correction evaluation using 18F-FDG human brain scans on a high-resolution PET scanner," *J. Nucl. Med.*, vol. 53, no. 3, pp. 495–504, 2012.

[243] J. E. M. Mourik, M. Lubberink, F. H. P. van Velden, A. A. Lammertsma, and R. Boellaard, "Off-line motion correction methods for multi-frame PET data," *Eur. J. Nucl. Med. Mol. Imag.*, vol. 36, no. 12, pp. 2002–2013, 2009.

[244] K. Thielemans, P. Schleyer, J. Dunn, P. K. Marsden, and R. M. Manjeshwar, "Using PCA to detect head motion from PET list mode data," in *Proc. IEEE Nucl. Sci. Symp. Med. Imag. Conf. Rec.*, 2013, pp. 1–5.

[245] J. Jiao, G. E. Searle, J. A. Schnabel, and R. N. Gunn, "Impact of image-based motion correction on dopamine D3/D2 receptor occupancy—Comparison of groupwise and frame-by-frame registration approaches," *EJNMMI Phys.*, vol. 2, no. 1. p. 15, 2015.

[246] T. Feng, D. Yang, W. Zhu, Y. Dong, and H. Li, "Real-time data-driven rigid motion detection and correction for brain scan with listmode PET," in *Proc. IEEE Nucl. Sci. Symp. Med. Imag. Conf. Room Temp. Semicond. Detector Workshop (NSS/MIC/RTSD)*, 2016, pp. 1–4.

[247] B. J. Lopresti *et al.*, "Implementation and performance of an optical motion tracking system for high resolution brain PET imaging," *IEEE Trans. Nucl. Sci.*, vol. 46, no. 6, pp. 2059–2067, Dec. 1999.

[248] C. Catana *et al.*, "MRI-assisted PET motion correction for neurologic studies in an integrated MR-PET scanner," *J. Nucl. Med.*, vol. 52, no. 1, pp. 154–161, Feb. 2011.

[249] G. J. Klein, B. W. Reutter, E. H. Botvinick, T. F. Budinger, and R. H. Huesman, "Fine-scale motion detection using intrinsic list mode PET information," in *Proc. IEEE Workshop Math. Methods Biomed. Image Anal.*, Kauai, HI, USA, 2001, pp. 71–78.

[250] Y. Lu *et al.*, "Data-driven voluntary body motion detection and non-rigid event-by-event correction for static and dynamic PET," *Phys. Med. Biol.*, vol. 64, no. 6, 2019, Art. no. 065002. doi: 10.1088/1361-6560/ab02c2.

[251] J. L. Andersson, "How to obtain high-accuracy image registration: Application to movement correction of dynamic positron emission tomography data," *Eur. J. Nucl. Med.*, vol. 25, no. 6, pp. 575–586, 1998.

[252] R. Klein, C. R. Hunter, R. S. Beanlands, and R. A. DeKemp, "Prevalence of patient motion in dynamic PET," *J. Nucl. Med.*, vol. 52, no. S1, p. 2105, May 2011.

[253] R. Fulton *et al.*, "Event-by-event motion compensation in 3D PET," in *Proc. IEEE Nucl. Sci. Symp. Conf. Rec.*, vols. 1–5, 2003, pp. 3286–3289.

[254] A. Rahmim *et al.*, "Motion compensation in histogram-mode and list-mode EM reconstructions: Beyond the event-driven approach," *IEEE Trans. Nucl. Sci.*, vol. 51, no. 5, pp. 2588–2596, Oct. 2004.

[255] K. Thielemans, C. Morel, M. W. Jacobson, J. H. Kaempf, and S. Mustafovic, "Normalisation of histogrammed list mode data," *IEEE Trans. Nucl. Sci.*, vol. 55, no. 1, pp. 543–551, Feb. 2008.

[256] V. W. Zhou, A. Z. Kyme, S. R. Meikle, and R. Fulton, "A scheme for PET data normalization in event-based motion correction," *Phys. Med. Biol.*, vol. 54, no. 17, pp. 5321–5339, 2009.

[257] A. Rahmim *et al.*, "Accurate event-driven motion compensation in high-resolution PET incorporating scattered and random events," *IEEE Trans. Med. Imag.*, vol. 27, no. 8, pp. 1018–1033, Aug. 2008.